

Resonant Ultrasound Spectroscopy for Irregularly Shaped Samples and Its Application to Uranium Ditelluride

Florian Theuss¹, Gregorio de la Fuente Simarro¹, Avi Shragai,¹ Gael Grisponnanche¹, Ian M. Hayes,² Shanta Saha,² Tatsuya Shishidou,³ Taishi Chen⁴, Satoru Nakatsuji,^{4,5,6,7} Sheng Ran,⁸ Michael Weinert,³ Nicholas P. Butch,^{2,9} Johnpierre Paglione,^{2,10} and B. J. Ramshaw^{1,10,*}

¹Laboratory of Atomic and Solid State Physics, Cornell University, Ithaca, New York 14853, USA

²Quantum Materials Center, Department of Physics, University of Maryland, College Park, Maryland 20742, USA

³Department of Physics, University of Wisconsin-Milwaukee, Milwaukee, Wisconsin 53201, USA

⁴The Institute for Solid State Physics, The University of Tokyo, Kashiwa, Chiba 277-8581, Japan

⁵Department of Physics, The University of Tokyo, Tokyo 113-0033, Japan

⁶Institute for Quantum Matter and Department of Physics and Astronomy, Johns Hopkins University, Baltimore, Maryland 21218, USA

⁷Trans-scale Quantum Science Institute, University of Tokyo, Tokyo 113-0033, Japan

⁸Department of Physics, Washington University in St. Louis, St. Louis, Missouri 63130, USA

⁹NIST Center for Neutron Research, National Institute of Standards and Technology,

100 Bureau Drive, Gaithersburg, Maryland 20899, USA

¹⁰Canadian Institute for Advanced Research, Toronto, Ontario, Canada



(Received 16 March 2023; revised 22 August 2023; accepted 11 January 2024; published 9 February 2024)

Resonant ultrasound spectroscopy (RUS) is a powerful technique for measuring the full elastic tensor of a given material in a single experiment. Previously, this technique was practically limited to regularly shaped samples such as rectangular parallelepipeds, spheres, and cylinders [W. M. Visscher *et al.* *J. Acoust. Soc. Am.* **90**, 2154 (1991)]. We demonstrate a new method for determining the elastic moduli of irregularly shaped samples, extending the applicability of RUS to a much larger set of materials. We apply this new approach to the recently discovered unconventional superconductor UTe₂ and provide its elastic tensor at both 300 and 4 kelvin.

DOI: 10.1103/PhysRevLett.132.066003

Introduction.—UTe₂ is a recently discovered unconventional superconductor [1] with upper critical fields as high as 65 tesla compared to a critical temperature that is at most 2 kelvin [1–3], and an nuclear magnetic resonance Knight shift [4–6] that suggest spin-triplet pairing. There are, however, many unsolved mysteries in UTe₂, including field-reentrant superconductivity [7–10], time-reversal symmetry breaking [11,12], a phase transition between superconducting ground states as a function of magnetic field [13], and the occurrence of two superconducting transitions in certain samples [12,14–16].

Externally applied stress has proven to be a useful tuning parameter when investigating these types of questions. For example, there are two unambiguous superconducting phase transitions in UTe₂ under hydrostatic pressure [10,17], and uniaxial pressure experiments [18] imply an insensitivity of the superconducting order parameter to shear strain. However, while stress and pressure are conceptually straightforward parameters to tune externally, the more physically relevant quantity—related to microscopic bond distances and unit cell volumes—is strain. Stress, σ , and strain, ϵ , are linearly related through the elastic tensor, $\sigma = c\epsilon$, and converting from the experimentally applied stress to strain requires the full elastic tensor. For example,

the full elastic tensor was central in determining the quantitative relationship between strain, the van Hove point, and superconductivity in Sr₂RuO₄ [19,20], as well as the relationship between anisotropic strains and superconductivity in CeIrIn₅ [21].

The full elastic tensor of a material can be determined with resonant ultrasound spectroscopy (RUS). RUS measures the mechanical resonance spectrum of a three-dimensional solid. The resonance frequencies are determined by both intrinsic sample properties—the density and elastic moduli—as well as by the sample boundary conditions. If the elastic moduli, density, and sample geometry are known, then the resonance frequencies are easily calculated numerically—the “forward problem”—either using the method of Visscher *et al.* [22] or by finite elements [23,24]. The inverse problem—obtaining the elastic moduli from a measured resonance spectrum—is more challenging because it requires multiple numerical evaluations of the forward problem and the navigation of a complex parameter landscape with many local minima [25].

For simple geometries with easily defined boundaries—typically rectangular parallelepipeds, cylinders, or spheres—the method of Visscher *et al.* [22] can be combined with either Levenberg-Marquardt or heuristic (such as genetic algorithm) fitting methods to solve the inverse problem and

obtain the elastic moduli from the resonance spectrum. For irregular samples, however, finite elements has been traditionally used to solve the forward problem [23,24]. The difficulty with this approach is that finite elements is too computationally intensive to use when solving the inverse problem. This has largely restricted the applicability of RUS to materials where regularly shaped samples can be prepared.

In the case of UTe_2 , preparation of a rectangular parallelepiped is difficult due to the brittle nature of the material (in addition to the potential hazards associated with polishing uranium compounds). In this Letter, we take advantage of the recent development by Shragai *et al.* [26] that solves the forward problem for irregularly shaped samples in a way that is two orders of magnitude faster than finite elements. This has allowed us to develop a protocol for solving the inverse problem for irregularly shaped samples. We demonstrate this protocol on single-crystal samples of SrTiO_3 and Mn_3Ge —compounds with known elastic moduli—and then apply our new technique to obtain the full elastic tensor of UTe_2 at 300 K and at 4 K.

Methods: Resonant ultrasound spectroscopy.—We performed RUS measurements by placing a sample in weak mechanical contact between two piezoelectric transducers, providing nearly free boundary conditions. One transducer is driven with an ac voltage at fixed frequency, and the voltage generated on the other transducer is measured using a lockin amplifier. By stepping the drive frequency from roughly 100 kHz to 5 MHz, we obtain the first 100 or so mechanical resonances for a typical, mm-scale sample. More details of the experimental setup and how to measure resonance spectra can be found in Ramshaw *et al.* [25] and Balakirev *et al.* [27]. Full lists of all experimental resonance spectra used in this Letter are given in the Supplemental Material (SM) [28].

Methods: Fitting resonance spectra.—Resonance spectra are calculated by minimizing the linear elastic Lagrangian as a function of the displacement field $\vec{u}(\vec{r}, t)$,

$$\mathcal{L} = \frac{1}{2} \int \left(\sum_i \rho \dot{u}_i^2(\vec{r}) - \sum_{ijkl} c_{ijkl} \frac{\partial u_i(\vec{r})}{\partial r_j} \frac{\partial u_k(\vec{r})}{\partial r_l} \right) dV, \quad (1)$$

where ρ is the density, c_{ijkl} is the elastic tensor, and the integral is over the entire volume of the sample. The widely adopted method of Visscher *et al.* [22] expands the displacements fields in a polynomial basis and solves the volume integrals analytically. This method only works for rectangular parallelepipeds, cylinders, spheres, or other regular shapes with analytically defined boundaries [22,27]. For irregularly shaped samples, however, this method is insufficient and new methods for computing the resonance spectra must be used.

We implement two resonance spectra calculation methods—two “forward” solvers—into a genetic algorithm, extending the RUS fitting routine to irregularly shaped samples. Details of the genetic algorithm itself can be found

in Ramshaw *et al.* [25] and in the SM [28]; here we focus on incorporating and verifying the new forward solvers to obtain the elastic moduli of UTe_2 .

The first forward solver extends Visscher’s method to irregular samples [26]. The displacement fields in Eq. (1) are expanded in the same polynomial basis as in Visscher *et al.* [22]. Instead of evaluating the integrals over the volume of the sample, however, we use Gauss’s law to project the integrals onto the surface of the sample. This allows us to evaluate the integrals for arbitrary shapes as long as the surface is encoded by a mesh of triangles. We will refer to fits performed with this forward solver as SMI (surface mesh integration [26]).

The second forward solver is a commercially available finite element solver: Comsol. We implement a Comsol forward solver to verify the use of the newer SMI method when fitting elastic moduli (i.e. when solving the inverse problem: the use of FEM to calculate the forward problem for RUS was described earlier in Liu and Maynard [23]). We will refer to fits performed using Comsol as the forward solver as FEM.

Both SMI- and FEM-based fits are compared to fits using Visscher’s approach for rectangular parallelepiped samples. Fits with Visscher’s approach are referred to as RPR. To facilitate comparison between the different methods, we fix the number of resonances to 70 (84) for all SrTiO_3 (Mn_3Ge) fits, and we expand the displacement field to 18th order for both the RPR and SMI methods (FEM does not expand the displacements in a polynomial basis).

Methods: Sample digitization and alignment.—Both the SMI and FEM methods require three-dimensional digitizations of the samples. FEM uses the full, three-dimensional tetrahedral mesh of the entire sample volume. SMI uses only the surface triangles of the same mesh (this includes any “interior” surfaces around voids). These digitizations were obtained with a Zeiss Xradia Versa XRM-520 X-ray nano-CT and are shown in Fig. 1. The mesh size used for our fits depends on the solver method, as well as on the sample shape and size. We use a mesh with average linear dimension 10 μm for SMI, and 60 μm for FEM (FEM uses a larger mesh because it is much more computationally intensive than SMI). The samples are oriented to within

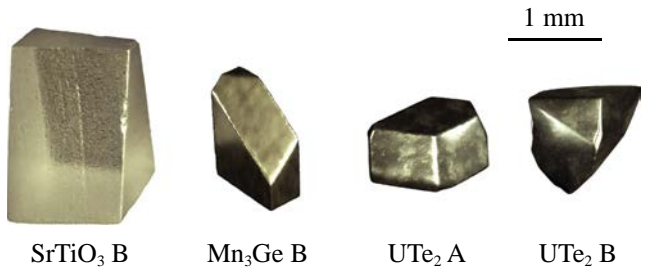


FIG. 1. CT scan models. 3D models of the irregularly shaped samples used for RUS measurements based on CT scans. From left to right: SrTiO_3 sample B, Mn_3Ge sample B, UTe_2 sample A, UTe_2 sample B.

1 degree using Laue backreflection diffractometry. The mesh is then aligned to the crystal axes by identifying two flat faces on the sample which uniquely relate the surface mesh to the orientation of the sample in the Laue apparatus. More details on sample digitization can be found in the SM [28].

Methods: Measurement uncertainty.—The quality of each fit is characterized by the root mean square (rms) of the difference between experimentally measured and calculated resonances. The uncertainties in the elastic moduli are estimated by calculating the change in elastic modulus needed to produce a 2% increase of the rms error [27,29].

We further identify three dominant systematic errors: (i) deviations from the weak-coupling approximation due to the weight of the transducer mount; (ii) uncertainty in the relative alignment between the sample mesh and the crystal axes; and (iii) uncertainty in the sample density. The first two of these each contribute a systematic uncertainty of approximately 1 GPa. The uncertainty in the density contributes an uncertainty of approximately 1%. We discuss these uncertainties in greater detail in the SM [28]. These systematic errors are general to RUS and not specific to the fitting methods implemented here.

Methods: Density functional theory calculations.—We used density-functional theory to produce estimates of the elastic moduli of UTe₂. This involved total energy calculations following the procedure of Ravindran *et al.* [32]. The full-potential linearized augmented plane wave method [33] calculations employed the generalized gradient approximation [34] for the exchange correlation, wave function, and potential energy cutoffs of 16 and 200 Ry, respectively, muffin-tin sphere radii of 1.35 Å, and an 8 × 8 × 8 *k*-point mesh. Spin-orbit coupling was fully taken into account in the assumed nonmagnetic state. The elastic tensor was extracted from fits of the total energy variations around the experimental structure [35] to the energy-strain formula [32], including linear terms. The resulting moduli are given in Table III.

Methods: Pulse-echo ultrasound.—We also measured the compressional and shear moduli of UTe₂ using a traditional pulse-echo ultrasound technique as outlined in Theuss *et al.* [36]. The elastic moduli are calculated by measuring the time between two successive sound echoes and using the known sample length and density. The uncertainty resulting in this analysis is dominated by a 5% uncertainty in sample thickness.

Test results.—We test the implementation of two forward solvers—FEM and SMI—for fitting the RUS spectra of irregularly shaped samples using a genetic algorithm. We compare these results to the moduli extracted for rectangular parallelepiped samples that can be fit using the RPR forward solver, in addition to the FEM and SMI methods. We find agreement between all methods and all sample geometries to within our measurement uncertainties. It is

worth noting that while both FEM and SMI are capable of fitting RUS spectra from irregularly shaped samples, the SMI method is two orders of magnitude faster than FEM, taking under an hour to produce a fit while FEM takes several days or even weeks.

SrTiO₃.—Our first test system for our new fitting method is SrTiO₃, whose elastic tensor consists of only three independent elements due to its cubic crystal structure (point group O_h). RUS measurements and fits are performed on two samples (Table I): Sample A was polished into a rectangular parallelepiped with dimensions (1.49 × 2.035 × 3.02) mm³, with edges oriented along the crystallographic axes. We can perform fits using all three methods—RPR, SMI, and FEM—in this simple geometry. Sample B was prepared with an irregular shape (see Fig. 1 for a 3D model based on a CT scan). Only SMI and FEM fits are possible for this geometry.

The fit results are given in Table I. We see that all methods yield identical results on the sample to within the given uncertainties. This demonstrates that, given the same experimental data and sample geometry, all three forward solvers implemented in a genetic algorithm yield the same elastic moduli. This is consistent with previous demonstrations that the three methods of forward computation—RPR, SMI, and FEM—are consistent to better than 1 part in 10⁴ [26]. Note, however, that both RPR and SMI are roughly a factor of 100 faster than the FEM method (details on fit performance and parameters for all fits can be found in the SM [28]).

TABLE I. Elastic moduli of SrTiO₃ in GPa. The elastic moduli for both SrTiO₃ samples. The sample polished into the shape of a rectangular parallelepiped is sample A, and the irregularly shaped sample is sample B. The uncertainties are from a 2% increase in rms fit error. Additional systematic errors are estimated to be on the order of 1 GPa each (see SM [28] for more details). Literature values are provided for comparison.

Sample	Fit method	c_{11}	c_{12}	c_{44}
SrTiO ₃ A	RPR	321.9	103.6	125.0
		±0.5	±0.6	±0.3
	FEM	321.9	103.6	125.0
		±0.5	±0.6	±0.3
	SMI	321.9	103.6	125.0
		±0.5	±0.6	±0.3
SrTiO ₃ B	FEM	316.7	103.1	121.9
		±0.5	±0.6	±0.3
	SMI	316.7	102.9	122.0
		±0.5	±0.6	±0.3
Bell and Rupprecht [37]		317	102	123
Poindexter and Giardini [38]		348	101	119
Lüthi and Moran [39]		331	105	126
Migliori <i>et al.</i> [29]		315	102	122
		±0.6	±0.7	±0.01

We find differences of less than 2.5% for all elastic moduli when comparing the rectangular parallelepiped (sample A) and irregular (sample B) samples. These differences are slightly larger than our statistical uncertainties. These deviations could be due to deviations of sample A from a perfect rectangular parallelepiped. All of our results are compatible within uncertainty to the measurements of Bell and Rupprecht [37] and Migliori *et al.* [29] (bottom rows of Table I). Both Poindexter and Giardini [38] and Lüthi and Moran [39] report values for c_{11} that are nearly 10% larger than the value we obtain. While this deviation is significantly larger than our uncertainties, it is consistent with the 10% error in absolute elastic moduli measured with pulse-echo ultrasound (the technique used in [39]; see our pulse-echo measurements on UTe₂ in Table III as a reference).

We observe that both the elastic moduli and their uncertainties are identical between different samples and solver methods. They are also consistent with the uncertainties measured in Migliori *et al.* [29]. We therefore conclude that our new fitting methods provide reliable elastic moduli, even for samples with irregular geometries.

Mn₃Ge.—Next, we test hexagonal Mn₃Ge, point group D_{6h} , which has five independent elastic moduli. Fit results are given in Table II. Similar to SrTiO₃, we show fit results for a rectangular parallelepiped sample (sample A) with dimensions (0.87 × 1.01 × 1.19) mm³ and corners parallel to high-symmetry directions, as well as an irregularly shaped sample (sample B, see Fig. 1 for a 3D model).

As with SrTiO₃, all fit methods yield the same moduli for Mn₃Ge for both samples to within measurement uncertainty. Our results for sample A are also in agreement with previously published elastic moduli of Mn₃Ge [40]. Comparing samples A and B, the absolute difference in elastic moduli is below 4 GPa. This value is consistent with our results for SrTiO₃ and is likely due to similar systematic uncertainties described above. Again, there is no significant difference in the resulting moduli or their uncertainties for the different fit methods (see Table II).

Application to UTe₂.—Having successfully demonstrated the extraction of elastic moduli from RUS spectra for irregularly shaped samples, we now fit for the elastic moduli of two irregularly shaped, single-crystal samples of UTe₂. Three-dimensional models of both samples are shown in Fig. 1, and the moduli are given in Table III.

UTe₂ is orthorhombic (point group D_{2h}), with nine independent elastic moduli. The population size—the number of initial guesses—required for a good fit using a genetic algorithm scales roughly linearly with the number of free parameters [30]. This means that the UTe₂ fits require nearly twice the population as compared to the previous Mn₃Ge fits. Additionally, the samples of SrTiO₃ and Mn₃Ge were produced by adding additional facets to what were previously rectangular parallelepiped samples, whereas our UTe₂ samples are as grown. This results in

TABLE II. Elastic moduli of Mn₃Ge in GPa. The elastic moduli for both Mn₃Ge samples. A rectangular parallelepiped is sample A, and the irregularly shaped sample is sample B. The uncertainties are from a 2% increase in rms fit error. Additional systematic errors are estimated to be on the order of 1 GPa each (see SM [28] for more details).

Sample	Fit method	c_{11}	c_{12}	c_{13}	c_{33}	c_{44}
Mn ₃ Ge A	RPR	130.0	43.9	13	202	48.3
		±0.3	±0.4	±2	±2	±0.2
	FEM	130.0	43.9	13	202	48.3
		±0.3	±0.3	±2	±2	±0.2
	SMI	130.0	43.9	13	202	48.3
		±0.3	±0.4	±2	±2	±0.2
Mn ₃ Ge B	FEM	126.8	40.3	14	203	48.7
		±0.3	±0.4	±4	±2	±0.2
	SMI	126.8	40.2	14	203	48.7
		±0.3	±0.4	±4	±2	±0.2

smaller feature sizes on the UTe₂ samples in comparison to the previous samples, requiring a finer mesh size for the 3D models (see SM [28] for details).

Both the dense mesh of our particular sample, and large number of moduli for UTe₂ in general, increase the fit time for the FEM method, which must recompute the entire spectrum at each stage of the fit. This makes FEM unsuitable for fitting elastic moduli, as convergence would take upward of a month. The SMI method, on the other hand, is largely unaffected by the increase in population size and mesh density because the computationally intensive step is performed only once, at the start of the fit, and the results are stored for use in subsequent generations of the genetic algorithm. We therefore only perform SMI fits to our UTe₂ spectra. This approach is justified by the results of the previous section, which demonstrated that fits using both FEM and SMI methods produce identical elastic moduli.

We find excellent agreement between the elastic moduli of UTe₂ samples A and B at both 300 K and 4 K (see Table III). For additional comparison, we present elastic moduli measured with pulse-echo ultrasound. We find no significant difference between these values and the ones obtained using RUS and we note that the uncertainties are greatly reduced using RUS. Also note that obtaining c_{12} , c_{13} , and c_{23} from pulse echo would require three additional experiments performed in different directions. We also report elastic moduli obtained from density-functional theory calculations (bottom row in Table III). These calculated values are in remarkable agreement with the experimental results. Other experimentally relevant quantities, including the bulk modulus, the Young's moduli, and the Poisson's ratios, are tabulated in the SM [28].

Conclusion.—We implement two methods for performing the forward calculation for resonance spectra into a genetic algorithm. These methods—SMI and FEM—allow

TABLE III. Elastic moduli of UTe₂ in GPa. The elastic moduli of UTe₂ samples A and B, shown in Fig. 1, at 300 K and at 4 K. The uncertainties are from a 2% increase in rms fit error. Additional systematic errors are estimated to be on the order of 1 GPa each (see SM [28] for more details). Also shown are the elastic moduli obtained with conventional pulse-echo ultrasound measurements, with uncertainties caused mainly by the uncertainty of the sample dimensions. Moduli obtained from DFT calculations, with atomic coordinates optimized, are given on the bottom row. The DFT values were used as rough guides to constrain the parameter space of the genetic algorithm fits to the RUS data.

	<i>T</i> (K)	<i>c</i> ₁₁	<i>c</i> ₂₂	<i>c</i> ₃₃	<i>c</i> ₁₂	<i>c</i> ₁₃	<i>c</i> ₂₃	<i>c</i> ₄₄	<i>c</i> ₅₅	<i>c</i> ₆₆
UTe ₂ A	4	90.3	144.1	95.9	25.7	41.3	31.9	28.05	53.2	30.43
		±0.2	±0.6	±0.2	±0.8	±0.2	±0.5	±0.08	±0.2	±0.08
	300	84.7	139.5	91.1	26.8	38.1	31.6	26.93	52.4	29.65
		±0.2	±0.5	±0.2	±0.6	±0.2	±0.5	±0.07	±0.2	±0.08
UTe ₂ B	4	89.2	146.9	94.0	28	40.4	31.4	28.2	52.5	30.3
		±0.3	±0.9	±0.3	±1	±0.2	±0.9	±0.1	±0.3	±0.1
	300	82.8	141.8	89.9	26	36.7	32.7	27.18	51.5	29.0
		±0.3	±0.8	±0.3	±1	±0.2	±0.7	±0.09	±0.3	±0.1
Pulse Echo	280	81	141	91	27	52	30
DFT		96	136	90	28	46	26	28	57	31

us to fit the elastic moduli of irregularly shaped samples using resonant ultrasound spectroscopy data. This is first demonstrated on materials with known elastic moduli (SrTiO₃ and Mn₃Ge), establishing consistency between our new methods and the older method of Visscher *et al.* [22], which is only applicable for regularly shaped samples. Our method is 100 times faster than an equivalent implementation using finite elements methods as the forward solver (see the SM [28] for timing details). We then apply our new method to measure the full elastic tensor of the unconventional superconductor UTe₂ at 300 K and at 4 K (Table III).

We expect that the elastic moduli of UTe₂ will be of use to researchers studying the superconducting properties under both uniaxial strain and hydrostatic pressure [9,10,15,17,18,41]. We expect that the general method that we have introduced—implementing the fast surface mesh integration method into a genetic algorithm—will be broadly useful for measuring the elastic moduli of samples that cannot be easily prepared into regular geometric shapes.

The code used to fit resonant ultrasound spectroscopy spectra is publicly available on GitHub [42].

Research at Cornell University was funded by the Office of Basic Energy Sciences of the U.S. Department of Energy under Award No. DE-SC0020143. Imaging data was acquired through the Cornell Institute of Biotechnology’s Imaging Facility, with NIH S10OD012287 for the ZEISS/Xradia Versa 520 X-ray Microscope (CT). Laue back-reflection diffraction measurements made use of the Cornell Center for Materials Research Shared Facilities which are supported through the NSF MRSEC program (DMR-1719875). Research at the University of Maryland

was supported by the Department of Energy under Award No. DE-SC-0019154 (sample characterization), the Gordon and Betty Moore Foundation’s EPiQS Initiative through Grant No. GBMF9071 (materials synthesis), NIST, and the Maryland Quantum Materials Center. Discussion of commercial software does not imply endorsement by NIST.

*bradramshaw@cornell.edu

- [1] S. Ran, C. Eckberg, Q.-P. Ding, Y. Furukawa, T. Metz, S. R. Saha, I.-L. Liu, M. Zic, H. Kim, J. Paglione, and N. P. Butch, Nearly ferromagnetic spin-triplet superconductivity, *Science* **365**, 684 (2019).
- [2] D. Aoki, A. Nakamura, F. Honda, D. Li, Y. Homma, Y. Shimizu, Y. J. Sato, G. Knebel, J.-P. Brison, A. Pourret, D. Braithwaite, G. Lapertot, Q. Niu, M. Vališka, H. Harima, and J. Flouquet, Unconventional superconductivity in heavy fermion UTe₂, *J. Phys. Soc. Jpn.* **88**, 043702 (2019).
- [3] S. Ran, S. R. Saha, I.-L. Liu, D. Graf, J. Paglione, and N. P. Butch, Expansion of the high field-boosted superconductivity in UTe₂ under pressure, *npj Quantum Mater.* **6**, 1 (2021).
- [4] G. Nakamine, S. Kitagawa, K. Ishida, Y. Tokunaga, H. Sakai, S. Kambe, A. Nakamura, Y. Shimizu, Y. Homma, D. Li, F. Honda, and D. Aoki, Superconducting properties of heavy fermion UTe₂ revealed by ¹²⁵Te-nuclear magnetic resonance, *J. Phys. Soc. Jpn.* **88**, 113703 (2019).
- [5] G. Nakamine, K. Kinjo, S. Kitagawa, K. Ishida, Y. Tokunaga, H. Sakai, S. Kambe, A. Nakamura, Y. Shimizu, Y. Homma, D. Li, F. Honda, and D. Aoki, Inhomogeneous superconducting state probed by ¹²⁵Te NMR on UTe₂, *J. Phys. Soc. Jpn.* **90**, 064709 (2021).
- [6] H. Fujibayashi, G. Nakamine, K. Kinjo, S. Kitagawa, K. Ishida, Y. Tokunaga, H. Sakai, S. Kambe, A. Nakamura, Y. Shimizu, Y. Homma, D. Li, F. Honda, and D. Aoki,

- Superconducting order parameter in UTe_2 determined by knight shift measurement, *J. Phys. Soc. Jpn.* **91**, 043705 (2022).
- [7] G. Knebel, W. Knafo, A. Pourret, Q. Niu, M. Vališka, D. Braithwaite, G. Lapertot, M. Nardone, A. Zitouni, S. Mishra, I. Sheikin, G. Seyfarth, J. P. Brison, D. Aoki, and J. Flouquet, Field-reentrant superconductivity close to a metamagnetic transition in the heavy-fermion superconductor UTe_2 , *J. Phys. Soc. Jpn.* **88**, 063707 (2019).
- [8] S. Ran, I. L. Liu, Y. S. Eo, D. J. Campbell, P. M. Neves, W. T. Fuhrman, S. R. Saha, C. Eckberg, H. Kim, D. Graf, F. Balakirev, J. Singleton, J. Paglione, and N. P. Butch, Extreme magnetic field-boosted superconductivity, *Nat. Phys.* **15**, 1250 (2019).
- [9] S. Ran, H. Kim, I.-L. Liu, S. R. Saha, I. Hayes, T. Metz, Y. S. Eo, J. Paglione, and N. P. Butch, Enhancement and reentrance of spin triplet superconductivity in UTe_2 under pressure, *Phys. Rev. B* **101**, 140503 (2020).
- [10] D. Aoki, F. Honda, G. Knebel, D. Braithwaite, A. Nakamura, D.X. Li, Y. Homma, Y. Shimizu, Y.J. Sato, J.P. Brison, and J. Flouquet, Multiple superconducting phases and unusual enhancement of the upper critical field in UTe_2 , *J. Phys. Soc. Jpn.* **89**, 053705 (2020).
- [11] D. S. Wei, D. Saykin, O. Y. Miller, S. Ran, S. R. Saha, D. F. Agterberg, J. Schmalian, N. P. Butch, J. Paglione, and A. Kapitulnik, Interplay between magnetism and superconductivity in UTe_2 , *Phys. Rev. B* **105**, 024521 (2022).
- [12] I. M. Hayes, D. S. Wei, T. Metz, J. Zhang, Y. S. Eo, S. Ran, S. R. Saha, J. Collini, N. P. Butch, D. F. Agterberg, A. Kapitulnik, and J. Paglione, Multicomponent superconducting order parameter in UTe_2 , *Science* **373**, 797 (2021).
- [13] A. Rosuel, C. Marcenat, G. Knebel, T. Klein, A. Pourret, N. Marquardt, Q. Niu, S. Rousseau, A. Demuer, G. Seyfarth, G. Lapertot, D. Aoki, D. Braithwaite, J. Flouquet, and J.-P. Brison, Field-induced tuning of the pairing state in a superconductor, [arXiv:2205.04524](https://arxiv.org/abs/2205.04524).
- [14] L. P. Cairns, C. R. Stevens, C. D. O'Neill, and A. Huxley, Composition dependence of the superconducting properties of UTe_2 , *J. Phys. Condens. Matter* **32**, 415602 (2020).
- [15] S. M. Thomas, C. Stevens, F. B. Santos, S. S. Fender, E. D. Bauer, F. Ronning, J. D. Thompson, A. Huxley, and P. F. S. Rosa, Spatially inhomogeneous superconductivity in UTe_2 , *Phys. Rev. B* **104**, 224501 (2021).
- [16] P. F. S. Rosa, A. Weiland, S. S. Fender, B. L. Scott, F. Ronning, J. D. Thompson, E. D. Bauer, and S. M. Thomas, Single thermodynamic transition at 2 K in superconducting UTe_2 single crystals, *Commun. Mater.* **3**, 33 (2022).
- [17] D. Braithwaite, M. Vališka, G. Knebel, G. Lapertot, J.-P. Brison, A. Pourret, M. E. Zhitomirsky, J. Flouquet, F. Honda, and D. Aoki, Multiple superconducting phases in a nearly ferromagnetic system, *Commun. Phys.* **2**, 147 (2019).
- [18] C. Girod, C. R. Stevens, A. Huxley, E. D. Bauer, F. B. Santos, J. D. Thompson, R. M. Fernandes, J.-X. Zhu, F. Ronning, P. F. S. Rosa, and S. M. Thomas, Thermodynamic and electrical transport properties of UTe_2 under uniaxial stress, *Phys. Rev. B* **106**, L121101 (2022).
- [19] M. E. Barber, F. Lechermann, S. V. Streletsov, S. L. Skornyakov, S. Ghosh, B. Ramshaw, N. Kikugawa, D. A. Sokolov, A. P. Mackenzie, C. W. Hicks *et al.*, Role of correlations in determining the Van Hove strain in Sr_2RuO_4 , *Phys. Rev. B* **100**, 245139 (2019).
- [20] Y.-S. Li, M. Garst, J. Schmalian, S. Ghosh, N. Kikugawa, D. A. Sokolov, C. W. Hicks, F. Jerzembeck, M. S. Ikeda, Z. Hu, B. J. Ramshaw, A. W. Rost, M. Nicklas, and A. P. Mackenzie, Elastocaloric determination of the phase diagram of Sr_2RuO_4 , *Nature (London)* **607**, 276 (2022).
- [21] M. D. Bachmann *et al.*, Spatial control of heavy-fermion superconductivity in CeIrIn_5 , *Science* **366**, 221 (2019).
- [22] W. M. Visscher, A. Migliori, T. M. Bell, and R. A. Reinert, On the normal modes of free vibration of inhomogeneous and anisotropic elastic objects, *J. Acoust. Soc. Am.* **90**, 2154 (1991).
- [23] G. Liu and J. Maynard, Measuring elastic constants of arbitrarily shaped samples using resonant ultrasound spectroscopy, *J. Acoust. Soc. Am.* **131**, 2068 (2012).
- [24] J. Plesek, R. Kolman, and M. Landa, Using finite element method for the determination of elastic moduli by resonant ultrasound spectroscopy, *J. Acoust. Soc. Am.* **116**, 282 (2004).
- [25] B. J. Ramshaw, A. Shekhter, R. D. McDonald, J. B. Betts, J. N. Mitchell, P. H. Tobash, C. H. Mielke, E. D. Bauer, and A. Migliori, Avoided valence transition in a plutonium superconductor, *Proc. Natl. Acad. Sci. U.S.A.* **112**, 3285 (2015).
- [26] A. Shragai, F. Theuss, G. Grissonnanche, and B. J. Ramshaw, Rapid method for computing the mechanical resonances of irregular objects, *J. Acoust. Soc. Am.* **153**, 119 (2023).
- [27] F. F. Balakirev, S. M. Ennaceur, R. J. Migliori, B. Maiorov, and A. Migliori, Resonant ultrasound spectroscopy: The essential toolbox, *Rev. Sci. Instrum.* **90**, 121401 (2019).
- [28] See Supplemental Material at <http://link.aps.org/supplemental/10.1103/PhysRevLett.132.066003> for all measured experimental resonance spectra, a detailed uncertainty analysis of our fits, and sample digitization details. We also tabulate values of bulk moduli, Young's moduli, and Poisson's ratios, as well as compare convergence times for the different forward solver methods. The supplement includes Refs. [18,22,25–27,29–31].
- [29] A. Migliori, J. L. Sarrao, W. M. Visscher, T. M. Bell, M. Lei, Z. Fisk, and R. G. Leisure, Resonant ultrasound spectroscopic techniques for measurement of the elastic moduli of solids, *Physica (Amsterdam)* **183B**, 1 (1993).
- [30] R. Storn and K. Price, Differential evolution: A simple and efficient heuristic for global optimization over continuous spaces, *J. Global Optim.* **11**, 341 (1997).
- [31] P. Virtanen *et al.* (SciPy1.0 Contributors), SciPy1.0: Fundamental algorithms for scientific computing in PYTHON, *Nat. Methods* **17**, 261 (2020).
- [32] P. Ravindran, L. Fast, P. A. Korzhavyi, B. Johansson, J. Wills, and O. Eriksson, Density functional theory for calculation of elastic properties of orthorhombic crystals: Application to TiSi_2 , *J. Appl. Phys.* **84**, 4891 (1998).
- [33] M. Weinert, G. Schneider, R. Podloucky, and J. Redinger, FLAPW: Applications and implementations, *J. Phys. Condens. Matter* **21**, 084201 (2009).
- [34] J. P. Perdew, K. Burke, and M. Ernzerhof, Generalized gradient approximation made simple, *Phys. Rev. Lett.* **77**, 3865 (1996).

- [35] S. Ikeda, H. Sakai, D. Aoki, Y. Homma, E. Yamamoto, A. Nakamura, Y. Shiokawa, Y. Haga, and Y. Ōnuki, Single crystal growth and magnetic properties of UTe₂, *J. Phys. Soc. Jpn.* **75**, 116 (2006).
- [36] F. Theuss, A. Shragai, G. Grissonnanche, I. M. Hayes, S. R. Saha, Y. S. Eo, A. Suarez, T. Shishidou, N. P. Butch, J. Paglione, and B. J. Ramshaw, Single-component superconductivity in UTe₂ at ambient pressure, [arXiv:2307.10938](https://arxiv.org/abs/2307.10938).
- [37] R. O. Bell and G. Rupprecht, Elastic constants of strontium titanate, *Phys. Rev.* **129**, 90 (1963).
- [38] E. Poindexter and A. A. Giardini, Elastic constants of strontium titanate (SrTiO₃), *Phys. Rev.* **110**, 1069 (1958).
- [39] B. Lüthi and T. J. Moran, Sound propagation near the structural phase transition in strontium titanate, *Phys. Rev. B* **2**, 1211 (1970).
- [40] F. Theuss, S. Ghosh, T. Chen, O. Tchernyshyov, S. Nakatsuji, and B. J. Ramshaw, Strong magnetoelastic coupling in Mn₃X (X = Ge, Sn), *Phys. Rev. B* **105**, 174430 (2022).
- [41] S. M. Thomas, F. B. Santos, M. H. Christensen, T. Asaba, F. Ronning, J. D. Thompson, E. D. Bauer, R. M. Fernandes, G. Fabbris, and P. F. S. Rosa, Evidence for a pressure-induced antiferromagnetic quantum critical point in intermediate-valence UTe₂, *Sci. Adv.* **6**, eabc8709 (2020).
- [42] https://github.com/CHILL-Ramshaw/rus_fitting.

Supplementary Information: Resonant Ultrasound Spectroscopy for Irregularly-Shaped Samples and its Application to Uranium Ditelluride

Florian Theuss,¹ Gregorio de la Fuente Simarro,¹ Avi Shragai,¹ Gael Grissonnanche,¹ Ian M Hayes,² Shanta Saha,² Tatsuya Shishidou,³ Taishi Chen,⁴ Satoru Nakatsuji,^{4, 5, 6, 7} Sheng Ran,⁸ Michael Weinert,³ Nicholas P Butch,^{2, 9} Johnpierre Paglione,^{2, 10} and B. J. Ramshaw^{1, 10, *}

¹Laboratory of Atomic and Solid State Physics, Cornell University, Ithaca, NY 14853, USA

²Quantum Materials Center, Department of Physics,

University of Maryland, College Park, Maryland 20742, USA

³Department of Physics, University of Wisconsin-Milwaukee, Milwaukee, Wisconsin 53201, USA

⁴The Institute for Solid State Physics, The University of Tokyo, Kashiwa, Chiba 277-8581, Japan

⁵Department of Physics, The University of Tokyo, Tokyo 113-0033, Japan

⁶Institute for Quantum Matter and Department of Physics and Astronomy,

Johns Hopkins University, Baltimore, MD 21218, USA

⁷Trans-scale Quantum Science Institute, University of Tokyo, Tokyo 113-0033, Japan

⁸Department of Physics, Washington University in St. Louis, St. Louis, MO 63130, USA

⁹NIST Center for Neutron Research, National Institute of Standards and Technology,

100 Bureau Drive, Gaithersburg, Maryland 20899, USA

¹⁰Canadian Institute for Advanced Research, Toronto, Ontario, Canada

(Dated: August 21, 2023)

I. BULK MODULUS, YOUNG'S MODULI, AND POISSON'S RATIOS

In Table I we present the bulk modulus B , the Young's moduli E_{ii} , and the Poisson's ratios ν_{ij} for all measured samples calculated from the elastic moduli shown in the main text (the fit results from fits using the SMI forward solver are used). For cubic SrTiO₃, all values are invariant under $x \leftrightarrow y \leftrightarrow z$, whereas for hexagonal Mn₃Ge, all values are invariant only under $x \leftrightarrow y$. For orthorhombic UTe₂, all moduli differ.

Sample	B (GPa)	Young's Moduli (GPa)			Poisson's Ratios					
		E_{xx}	E_{yy}	E_{zz}	ν_{xz}	ν_{zx}	ν_{yz}	ν_{zy}	ν_{xy}	ν_{yx}
SrTiO ₃	A	176.4	271.5	-	-	0.243	-	-	-	-
	B	174.2	266.1	-	-	0.245	-	-	-	-
Mn ₃ Ge	A	66.0	114.8	-	200	0.042	0.07	-	-	0.334
	B	65	113.5	-	200	0.05	0.08	-	-	0.312
UTe ₂	300 K	55.0	67.4	125.9	71.1	0.382	0.402	0.265	0.150	0.105
	4 K	57.5	71.5	131.5	74.0	0.401	0.415	0.262	0.147	0.090
UTe ₂	300 K	54.2	66.6	127	70.3	0.372	0.393	0.29	0.159	0.098
	4 K	57.4	70.3	133	73.1	0.395	0.411	0.25	0.135	0.107
										0.19

TABLE I. **Elastic properties.** Bulk modulus, Young's moduli, and Poisson's ratios of all measured samples determined from RUS fits using the SMI forward solver.

II. DENSITY FUNCTIONAL THEORY

In Table II we compare the elastic moduli from density functional theory obtained from calculations during which the atomic coordinates were frozen to experimental values to calculations in which they were optimized. We also compare to calculations presented in the supplement of Girod *et al.* [1].

III. SAMPLE DIGITIZATION

Three-dimensional digitizations of the samples were obtained with a Zeiss Xradia Versa XRM-520 X-ray nano-CT. The average mesh size (see Table III) varies between samples and RUS solver methods (i.e. SMI vs. FEM). We used

* bradramshaw@cornell.edu

Method	c_{11}	c_{22}	c_{33}	c_{12}	c_{13}	c_{23}	c_{44}	c_{55}	c_{66}
coordinates frozen	100.2	140.0	99.3	28.7	56.4	27.1	33.8	69.4	36.1
coordinates optimized	95.7	136.0	89.7	28.1	46.0	26.0	28.0	57.1	31.0
Girod et al. [1]	97.0	140.7	101.3	40.9	48.6	46.7	19.6	57.3	27.1

TABLE II. **UTe₂ DFT elastic tensor.** Presented are the elastic moduli from density functional theory calculations. The first two rows are our calculations with atomic coordinates frozen to the experimental values and optimized. The last row are values given in the SI of [1], where the atomic coordinates were allowed to relax during minimization.

smaller meshes for irregularly-shaped samples (compared to regularly shaped ones) as well as for fits using the SMI method (compared to the FEM method). The latter is because a smaller mesh size increases the time for a fit to converge significantly for the FEM method, but leaves it almost unaffected for the SMI method [2].

Figure 1 shows the meshes used for fits performed with the FEM forward solver (meshes for fits performed with the SMI method are too dense to be resolved at this scale).

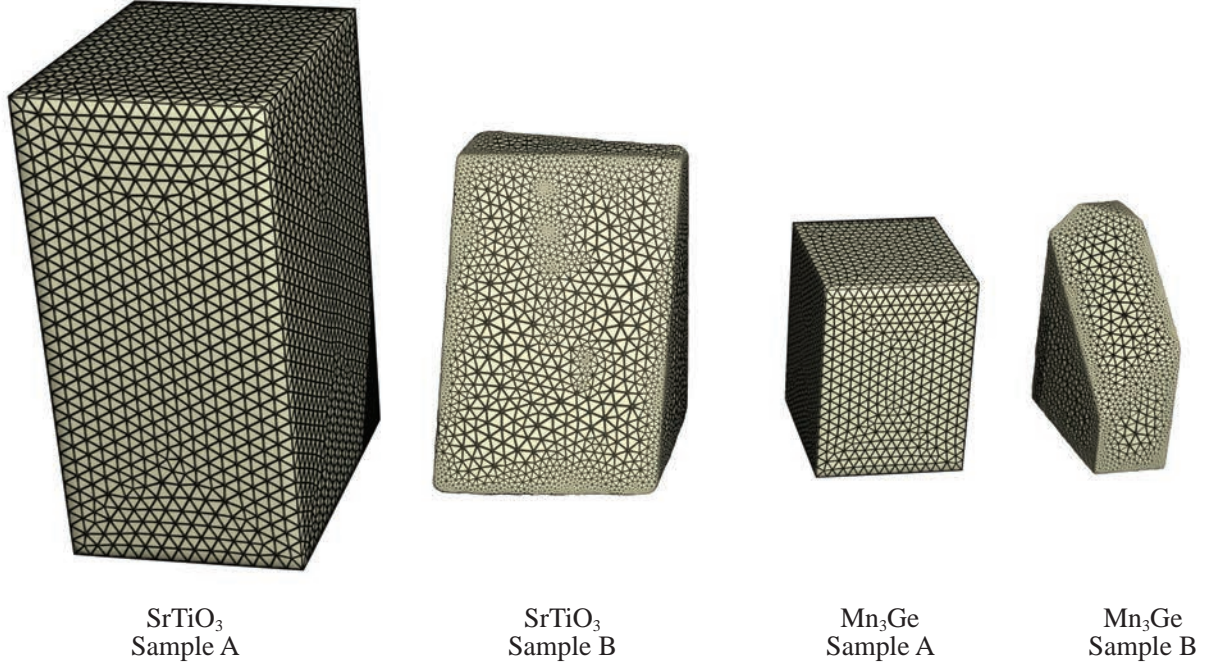


FIG. 1. **CT-Scan Meshes.** Shown are (from left to right) the digitizations for the SrTiO₃ (samples A, B) and Mn₃Ge (samples A, B) samples used for the RUS fits with the FEM method. Meshes for fits using the SMI method are too dense for individual faces to be identifiable on the shown scale.

Method	SrTiO ₃ sample A	SrTiO ₃ sample B	Mn ₃ Ge sample A	Mn ₃ Ge sample B	UTe ₂ sample A	UTe ₂ sample B
FEM	103	40	63	30	-	-
SMI	60	5	23	5	9	4

TABLE III. **Mesh Size.** Average distance between two vertices (in μm) in the meshes used in the RUS fits.

IV. GENETIC ALGORITHM

We use a genetic algorithm global minimizer to extract the elastic moduli from the experimental resonance spectra [3–5]. A genetic algorithm is initialized with its first generation by randomly generating N sets of elastic moduli within given bounds. We call these sets parent sets, x_i^{parent} , $i \in [1, 2, \dots, N]$. Here every x_i^{parent} is a vector containing the independent elastic moduli of a given material. A resonance spectrum is then calculated for all parent sets

(see discussion below on details on how resonances are calculated), and compared to the experimental resonance frequencies. The best set of elastic moduli x_i^{best} is characterized by the lowest χ^2 value. The second generation of the genetic algorithm is then created in three steps: First, a mutated set of elastic moduli x_i^{mut} is constructed for every parent set x_i^{parent} through

$$x_i^{mut} = x_i^{best} + \epsilon (x_j^{parent} + x_k^{parent}). \quad (1)$$

Here, $j, k \in [1, N]$ are random indices, and the mutation parameter $\epsilon \in [0, 2]$ ensures a controlled perturbation of x_i^{best} . Secondly, trial sets x_i^{trial} are created from each mutated parameter set. For this procedure, each element $x_{i,j}^{trial}$ —i.e. each elastic modulus—of a given trial set is constructed as

$$x_{i,j}^{trial} = \begin{cases} x_{i,j}^{mut} & \text{if } rand(j) \leq p \text{ or } j = d \\ x_{i,j}^{parent} & \text{if } rand(j) > p \end{cases}, \quad (2)$$

where $rand(j) \in [0, 1]$ is a random number, $p \in [0, 1]$ is the crossover probability, and d is the number of elastic moduli. In the last step, each original parent set x_i^{parent} is compared to its related trial set x_i^{trial} and the set with smallest χ^2 value is chosen for the next generation. This procedure is repeated until the standard deviation of the residuals of a given generation falls below a predetermined tolerance level. The quality of this fit can be improved further by performing a gradient descent fit, using the results of the genetic algorithm as starting parameters.

The genetic parameters used for our fits are a population size of $N = 15 * n$, where n is the number of elastic moduli, a mutation parameter $\epsilon = 0.7$, and a crossover probability $p = 0.9$.

V. RUS FIT UNCERTAINTIES

Statistical uncertainties in a RUS fit are typically determined by the following procedure [6, 7]. A root mean square (RMS) error of the differences between the measured resonances and the resonances calculated from the best fit. The uncertainty of each elastic modulus is then determined by calculating what change in elastic modulus causes an increase of the RMS by 2 %. These uncertainties are the ones given in the main text.

Additionally, we identify three main sources of systematic uncertainty in our fits, which are of similar magnitude as our statistical uncertainties. They are due to small deviations from the weak-coupling approximation used in our analysis, from small uncertainties in the alignment between the crystal axes and the sample mesh, and due to uncertainties in the sample densities.

The first source of systematic uncertainty is caused by the weight of the cantilever holding the top ultrasonic transducer and causes the measured resonance frequencies to weakly depend on how the sample is mounted in the RUS apparatus. To estimate the resulting uncertainty in elastic moduli, we arranged all irregularly-shaped samples in three different ways between the transducers and re-performed RUS measurements and fits. Figure 2 illustrates the different arrangements of samples in the setup and the rows in Table IV show the respective elastic moduli (note that arrangement 2 is how the samples were mounted for the results shown in the main paper). This analysis leads to an average uncertainty of 1.7 GPa, 2.3 GPa, 0.5 GPa for SrTiO₃ sample B, Mn₃Ge sample B, and UTe₂ sample A at 300 K, respectively. The uncertainties for the SrTiO₃ and Mn₃Ge samples are about a factor of 4 larger than for the UTe₂ sample. We attribute this difference to the different RUS apparatus used to measure those samples. SrTiO₃ and Mn₃Ge samples were measured in a RUS setup with a cantilever weighing about 5 g, while the UTe₂ spectra were recorded in an apparatus with a cantilever weighing about 0.5 g.

The second systematic contribution originates in an uncertainty of about 1 degree to which we can align the crystal axes and the sample mesh using Laue backreflection diffractometry. Refitting our RUS resonance spectra with a sample mesh rotated by 1 degree results in difference of 0.4 GPa, 2 GPa, 0.5 GPa, for the elastic moduli of SrTiO₃ sample B, Mn₃Ge sample B, and UTe₂ sample A at 300 K, respectively. Individual error bars for each elastic modulus due to sample misalignment are given in Table IV.

The third source of systematic uncertainty comes from uncertainty in the sample density. We estimate this contribution to be on the order of 1 % for all elastic moduli equally, based on the difference between measured densities and literature values.

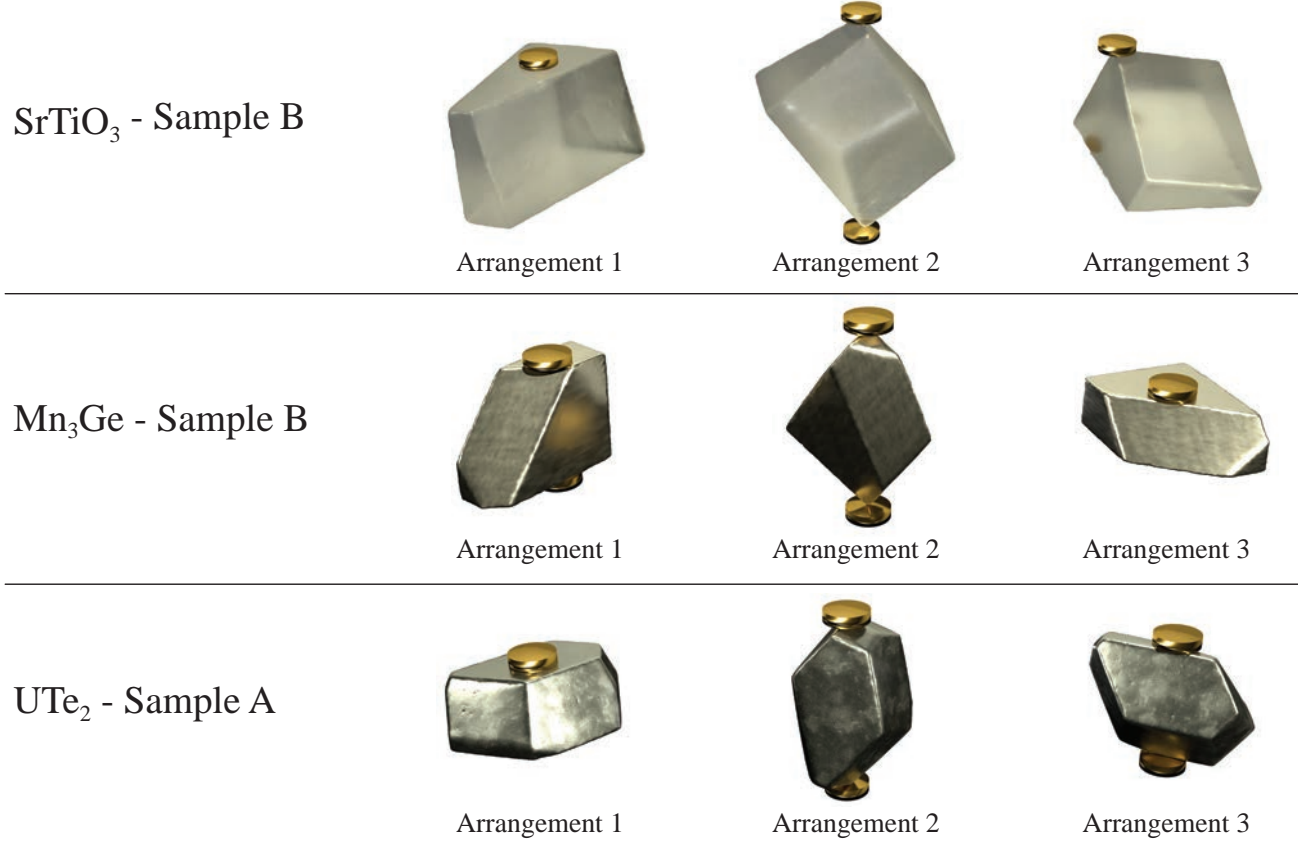


FIG. 2. RUS Sample Arrangements. Shown are different arrangements of the samples in the RUS apparatus. The golden discs represent the ultrasonic transducers (the bottom transducer is occluded by the sample in some images). The arrangement number relates to the correct row in [Table IV](#).

Sample	Arrangement	c_{11}	c_{22}	c_{33}	c_{12}	c_{13}	c_{23}	c_{44}	c_{55}	c_{66}
SrTiO_3 B	1	313.8	-	-	100.3	-	-	122.62	-	-
	2	316.7 ± 0.5	-	-	102.9 ± 0.7	-	-	121.95 ± 0.05	-	-
	3	315.8	-	-	100.2	-	-	122.30	-	-
Mn_3Ge B	1	126	-	200	38	12	-	48.7	-	-
	2	127 ± 1	-	203 ± 2	40 ± 2	14 ± 5	-	48.7 ± 0.5	-	-
	3	129	-	196	42	18	-	49.6	-	-
UTe_2 A (300 K)	1	84.4	139.0	92.0	25.6	38.1	32.0	26.9	52.3	29.4
	2	84.7 ± 0.44	139.5 ± 0.8	91.1 ± 1.1	26.8 ± 1.0	38.1 ± 0.5	31.6 ± 0.4	26.9 ± 0.2	52.4 ± 0.2	29.7 ± 0.2
	3	83.8	140.3	90.6	25.5	37.2	31.6	27.1	52.3	29.4

TABLE IV. RUS Uncertainty Analysis. Elastic moduli in GPa for the different arrangements of all irregularly-shaped samples shown in [Figure 2](#) to estimate the uncertainty introduced by the weight of the cantilever holding the top ultrasonic transducer. For each sample and arrangement 2, we also show the errors caused by a 1 degree misalignment between the crystal axes and the sample mesh. All fits were performed with the SMI method.

VI. INTRODUCTION TO RUS FORWARD SOLVERS

Here, we briefly introduce the three different forward solvers (RPR, SMI, and FEM) used in our fits to highlight their similarities and differences. A detailed derivation of the RPR forward solver can be found in [6–8] and the SMI method is described in detail in Shragai *et al.* [2].

Both RPR and SMI methods are based on the linear elastic Lagrangian

$$\mathcal{L} = \frac{1}{2} \int \left(\sum_i \rho \dot{u}_i^2(\vec{r}, t) - \sum_{ijkl} c_{ijkl} \frac{\partial u_i(\vec{r}, t)}{\partial r_j} \frac{\partial u_k(\vec{r}, t)}{\partial r_l} \right) dV, \quad (3)$$

where ρ is the density, c_{ijkl} is the elastic tensor, the integral is over the entire volume of the sample, and the free variable is the displacement field $\vec{u}(\vec{r}, t)$. Assuming a periodic time dependence of the displacement field $\vec{u}(\vec{r}, t) = e^{i\omega t} \vec{u}(\vec{r})$ and expanding its spatial component in terms of Cartesian polynomials

$$u_i = \sum_{\lambda} a_{i,\lambda} \phi_{\lambda}, \quad (4)$$

where $\phi_{\lambda} = x^n y^m z^l$, the Lagrangian in [Equation 3](#) can be rewritten as

$$\mathcal{L} = \frac{1}{2} \omega^2 \mathbf{a}^T \mathbf{E} \mathbf{a} - \frac{1}{2} \mathbf{a}^T \mathbf{\Gamma} \mathbf{a}. \quad (5)$$

Displacement vectors which are stationary solutions to the Lagrangian are then given by the generalized eigenvalue equation

$$\omega^2 \mathbf{E} \mathbf{a} = \mathbf{\Gamma} \mathbf{a}. \quad (6)$$

The kinetic energy matrix \mathbf{E} and the potential energy matrix $\mathbf{\Gamma}$ in [Equation 5](#) and [Equation 6](#) are expressed by

$$E_{\lambda i \lambda' i'} = \delta_{ii'} \int_V \phi_{\lambda} \rho \phi_{\lambda'} dV, \quad (7)$$

$$\Gamma_{\lambda i \lambda' i'} = c_{iji'j'} \int_V \frac{\partial \phi_{\lambda}}{\partial x_j} \frac{\partial \phi_{\lambda'}}{\partial x_{j'}} dV. \quad (8)$$

Note that due to our choice of basis, [Equation 7](#) and [Equation 8](#) are simply integrals of Cartesian polynomials. Evaluating these integrals is thus straightforward for samples with regular shapes, which is what is done using the RPR method. Once the \mathbf{E} and $\mathbf{\Gamma}$ matrices are calculated, the resonance frequencies ω can be obtained by solving the generalized eigenvalue problem in [Equation 6](#) with standard numerical eigenvalue solvers.

The SMI method is based on the same Lagrangian as the RPI method. The displacement field is still expanded in Cartesian polynomials and resonances are still computed by solving the generalized eigenvalue problem in [Equation 6](#). The difference is in the way the kinetic and potential energy matrices \mathbf{E} and $\mathbf{\Gamma}$ are calculated. Because we choose to expand the displacement field in Cartesian coordinates, the integrals in [Equation 7](#) and [Equation 8](#) are of the general form $\int x^m y^n z^l dV$. These volume integrals can be rewritten as surface integrals according to the following:

$$\int_V x^m y^n z^l dV = \frac{1}{l+1} \int_V \nabla \cdot (0, 0, x^m y^n z^{l+1}) dV \quad (9)$$

$$= \frac{1}{l+1} \int_A d\vec{A} \cdot (0, 0, x^m y^n z^{l+1}), \quad (10)$$

where we have used Gauss' law in the second step. The integral in [Equation 10](#) is now over the surface of the sample, rather than its volume. The kinetic and potential energy matrices required for the generalized eigenvalue problem [Equation 6](#) can thus be created by integrating Cartesian polynomials over the surface of a sample, which can be done numerically for any surface digitized with a triangular mesh.

Here it should be emphasized again that RPR and SMI methods are based on the same idea: By expanding the displacement field in terms of Cartesian polynomials, stationary solutions to the elastic Lagrangian [Equation 3](#) can be found by solving the generalized eigenvalue problem [Equation 6](#). The only difference between RPR and SMI methods is in the way the matrices in [Equation 6](#) are created. In all our fits (i.e. for all samples, and RPR and SMI methods), the displacement field was expanded in polynomials up to order 18.

The last method, FEM, stands for *finite element method* and utilizes the commercially available finite element solver Comsol.

We compare the performance of the three forward methods by recording the time it takes for a fit to converge and dividing it by the total number of evaluations of the target function. This gives us the average computation time for one forward calculation, as the forward calculation time dominates the fitting procedure (see [Table V](#)). The times recorded in [Table V](#) are taken from fits performed on an Intel® Xenon® Gold 2.10 GHz processor, parallelized over 40 cores. We perform this analysis for samples SrTiO₃ A and Mn₃Ge A, for which fits with all three methods are available.

Sample	RPR	SMI	FEM
SrTiO ₃ sample A	0.9	0.9	92
Mn ₃ Ge sample A	0.9	0.9	40

TABLE V. **Fit Performance.** Average time in seconds it takes for the evaluation of one forward calculation during RUS fits for samples SrTiO₃ A and Mn₃Ge A and for all forward solver methods.

We find no significant difference between the solver methods or the two samples when comparing the performance for RPR and SMI methods. This is as expected because of the strong similarities of both forward methods as outlined above. The time-consuming step in the calculation of resonance spectra is solving the generalized eigenvalue problem in [Equation 6](#) and is identical for both RPR and SMI methods. It is also identical between different samples, as long as the polynomial expansion in [Equation 4](#) is truncated at the same order (we used an expansion to order 18 for all fits using RPR and SMI methods).

Times for the FEM solver are two orders of magnitude longer. The time it takes the FEM solver to calculate one forward step in our fit is influenced by the mesh size chosen for the digitization of the sample and by the number of resonances computed. Both contributions differ from sample to sample, which explains the difference between the computation times of SrTiO₃ and Mn₃Ge samples using the FEM forward solver.

VII. RUS RESONANCES SPECTRA AND FIT RESULTS

We show lists of experimental resonance frequencies f_{exp} along with the calculated frequencies f_{calc} corresponding to the RUS fit results in the main text. The lowest three resonances are excluded from all fits. We used 70 resonances for all SrTiO₃ fits and 84 resonances for all Mn₃Ge fits. For the UTe₂ fits, we included 140 (150) resonances for sample A at 300 K (4 K) and 114 (118) resonances for sample B at 300 K (4 K).

TABLE VI: SrTiO₃ sample A (regular shape)

Index	f_{exp} (MHz)	RPR		SMI		FEM	
		f_{calc} (MHz)	diff (%)	f_{calc} (MHz)	diff (%)	f_{calc} (MHz)	diff (%)
1	0.71037	0.70491	-	0.70491	-	0.70489	-
2	0.79197	0.79156	-	0.79156	-	0.79155	-
3	0.89772	0.90185	-	0.90185	-	0.90184	-
4	1.17353	1.17781	0.363	1.17781	0.363	1.17779	0.361
5	1.24570	1.24714	0.116	1.24714	0.116	1.24711	0.113
6	1.33132	1.32506	0.473	1.32506	0.473	1.32504	0.474
7	1.37709	1.38138	0.310	1.38138	0.310	1.38135	0.308
8	1.41735	1.40410	0.944	1.40410	0.944	1.40408	0.945
9	1.50363	1.49941	0.281	1.49941	0.281	1.49939	0.283
10	1.55724	1.55327	0.256	1.55327	0.256	1.55325	0.257
11	1.59727	1.58515	0.765	1.58515	0.765	1.58513	0.766
12	1.60045	1.58865	0.743	1.58865	0.743	1.58863	0.744
13	1.71219	1.71178	0.024	1.71178	0.024	1.71175	0.025
14	1.77642	1.77451	0.108	1.77451	0.108	1.77449	0.109
15	1.78574	1.79251	0.377	1.79251	0.377	1.79247	0.375
16	1.83710	1.84222	0.278	1.84222	0.277	1.84219	0.276
17	1.85498	1.85528	0.016	1.85528	0.016	1.85524	0.014
18	1.91594	1.92356	0.396	1.92356	0.396	1.92353	0.395
19	1.97811	1.97315	0.251	1.97315	0.251	1.97314	0.252
20	1.98353	1.98541	0.095	1.98541	0.095	1.98538	0.093
21	2.03547	2.04563	0.496	2.04563	0.496	2.04559	0.495
22	2.07281	2.07985	0.338	2.07985	0.338	2.07982	0.337
23	2.16306	2.17696	0.638	2.17696	0.639	2.17695	0.638
24	2.17570	2.17867	0.136	2.17867	0.136	2.17864	0.135
25	2.20327	2.21156	0.375	2.21156	0.375	2.21154	0.374

Table 6 continued on next page.

Table 6 continued.

Index	f_{exp} (MHz)	RPR		SMI		FEM	
		f_{calc} (MHz)	diff (%)	f_{calc} (MHz)	diff (%)	f_{calc} (MHz)	diff (%)
26	2.20830	2.21607	0.350	2.21607	0.350	2.21606	0.350
27	2.22903	2.22728	0.078	2.22728	0.078	2.22727	0.079
28	2.23226	2.23763	0.240	2.23763	0.240	2.23761	0.239
29	2.23351	2.23846	0.221	2.23846	0.221	2.23845	0.221
30	2.28139	2.27258	0.388	2.27258	0.388	2.27258	0.388
31	2.32126	2.31051	0.465	2.31051	0.465	2.31052	0.465
32	2.33100	2.32182	0.395	2.32182	0.395	2.32180	0.396
33	2.34719	2.34083	0.272	2.34083	0.272	2.34082	0.272
34	2.44146	2.44675	0.216	2.44675	0.216	2.44674	0.216
35	2.46013	2.45143	0.355	2.45142	0.355	2.45144	0.355
36	2.50210	2.50958	0.298	2.50958	0.298	2.50956	0.297
37	2.50662	2.50968	0.122	2.50968	0.122	2.50965	0.121
38	2.53756	2.53887	0.051	2.53887	0.051	2.53889	0.052
39	2.57650	2.57679	0.011	2.57679	0.011	2.57680	0.012
40	2.58500	2.59496	0.384	2.59496	0.384	2.59496	0.384
41	2.59850	2.59922	0.028	2.59922	0.028	2.59920	0.027
42	2.62865	2.63115	0.095	2.63116	0.095	2.63117	0.096
43	2.65167	2.65229	0.023	2.65229	0.023	2.65226	0.022
44	2.68309	2.68338	0.011	2.68338	0.011	2.68338	0.011
45	2.70518	2.70901	0.141	2.70901	0.141	2.70898	0.140
46	2.74782	2.74881	0.036	2.74881	0.036	2.74883	0.037
47	2.75176	2.75107	0.025	2.75107	0.025	2.75107	0.025
48	2.75392	2.76091	0.253	2.76091	0.253	2.76092	0.254
49	2.78789	2.79403	0.220	2.79403	0.220	2.79408	0.221
50	2.80071	2.79544	0.189	2.79545	0.188	2.79545	0.188
51	2.82197	2.82346	0.053	2.82346	0.053	2.82352	0.055
52	2.84439	2.85166	0.255	2.85167	0.255	2.85166	0.255
53	2.91635	2.91928	0.101	2.91928	0.101	2.91931	0.102
54	2.92322	2.92473	0.051	2.92473	0.051	2.92478	0.053
55	2.94885	2.92904	0.677	2.92904	0.677	2.92902	0.677
56	3.00333	2.99929	0.135	2.99929	0.135	2.99940	0.131
57	3.01642	3.01070	0.190	3.01070	0.190	3.01074	0.189
58	3.03353	3.03246	0.035	3.03246	0.036	3.03254	0.033
59	3.03869	3.04328	0.151	3.04328	0.151	3.04332	0.152
60	3.06889	3.06572	0.103	3.06572	0.103	3.06574	0.103
61	3.13815	3.14283	0.149	3.14283	0.149	3.14288	0.151
62	3.15099	3.15332	0.074	3.15332	0.074	3.15339	0.076
63	3.15918	3.16111	0.061	3.16111	0.061	3.16112	0.062
64	3.16664	3.16975	0.098	3.16975	0.098	3.16985	0.101
65	3.22486	3.22895	0.127	3.22895	0.127	3.22893	0.126
66	3.22600	3.23110	0.158	3.23110	0.158	3.23107	0.157
67	3.25102	3.24020	0.334	3.24020	0.334	3.24033	0.330
68	3.25333	3.24905	0.132	3.24905	0.132	3.24915	0.129
69	3.26656	3.25129	0.470	3.25129	0.470	3.25141	0.466
70	3.27348	3.28127	0.237	3.28127	0.237	3.28131	0.239

TABLE VII: SrTiO₃ sample B (irregular shape)

Index	f_{exp} (MHz)	SMI		FEM	
		f_{calc} (MHz)	diff (%)	f_{calc} (MHz)	diff (%)
1	1.10869	1.09168	-	1.09156	-
2	1.20480	1.19121	-	1.19112	-
3	1.52331	1.50347	-	1.50341	-
4	1.88059	1.86636	0.762	1.86620	0.771
5	1.97243	1.97144	0.050	1.97135	0.055
6	1.98450	1.98777	0.164	1.98756	0.154
7	2.07997	2.07118	0.424	2.07100	0.433
8	2.15054	2.14467	0.274	2.14453	0.280
9	2.23955	2.23207	0.335	2.23186	0.344
10	2.37823	2.36840	0.415	2.36833	0.418
11	2.43553	2.44027	0.194	2.44001	0.184

Table 7 continued on next page.

Table 7 continued.

Index	f_{exp} (MHz)	SMI		FEM	
		f_{calc} (MHz)	diff (%)	f_{calc} (MHz)	diff (%)
12	2.58487	2.57275	0.471	2.57258	0.478
13	2.72511	2.71927	0.215	2.71912	0.220
14	2.80098	2.79093	0.360	2.79078	0.366
15	2.83415	2.83210	0.072	2.83199	0.077
16	2.87280	2.86311	0.339	2.86304	0.341
17	2.92701	2.91494	0.414	2.91473	0.421
18	3.07796	3.07446	0.114	3.07432	0.118
19	3.13235	3.14863	0.517	3.14864	0.517
20	3.16734	3.16494	0.076	3.16486	0.079
21	3.18282	3.18195	0.027	3.18191	0.029
22	3.25382	3.24307	0.331	3.24298	0.334
23	3.29615	3.29027	0.179	3.29022	0.180
24	3.31731	3.33535	0.541	3.33524	0.538
25	3.48056	3.50474	0.690	3.50469	0.688
26	3.51006	3.52415	0.400	3.52412	0.399
27	3.65645	3.66182	0.147	3.66178	0.145
28	3.78318	3.79193	0.231	3.79191	0.230
29	3.84523	3.84207	0.082	3.84198	0.085
30	3.89894	3.90375	0.123	3.90368	0.122
31	3.98772	3.99729	0.239	3.99727	0.239
32	4.00064	4.00409	0.086	4.00407	0.086
33	4.06006	4.04985	0.252	4.04979	0.254
34	4.10005	4.10447	0.108	4.10444	0.107
35	4.15255	4.14028	0.296	4.14022	0.298
36	4.18979	4.20182	0.286	4.20174	0.284
37	4.23696	4.22814	0.209	4.22819	0.207
38	4.27449	4.28863	0.330	4.28857	0.328
39	4.30861	4.31115	0.059	4.31124	0.061
40	4.34986	4.35327	0.078	4.35335	0.080
41	4.39819	4.39097	0.165	4.39113	0.161
42	4.46403	4.46713	0.069	4.46719	0.071
43	4.48597	4.47481	0.249	4.47493	0.247
44	4.63845	4.62951	0.193	4.62957	0.192
45	4.68243	4.69013	0.164	4.69022	0.166
46	4.74359	4.74395	0.008	4.74417	0.012
47	4.75697	4.76987	0.270	4.76996	0.272
48	4.80223	4.79540	0.142	4.79552	0.140
49	4.82394	4.84266	0.387	4.84274	0.388
50	4.89389	4.90448	0.216	4.90445	0.215
51	4.93746	4.93653	0.019	4.93677	0.014
52	4.98372	4.98686	0.063	4.98700	0.066
53	5.00140	5.00252	0.022	5.00247	0.021
54	5.03260	5.03444	0.037	5.03457	0.039
55	5.06065	5.06660	0.117	5.06673	0.120
56	5.10892	5.10434	0.090	5.10460	0.085
57	5.12704	5.12970	0.052	5.12991	0.056
58	5.16940	5.18029	0.210	5.18061	0.216
59	5.20187	5.23093	0.556	5.23130	0.562
60	5.25259	5.25272	0.002	5.25278	0.004
61	5.27776	5.27884	0.020	5.27913	0.026
62	5.28863	5.29927	0.201	5.29969	0.209
63	5.33266	5.33158	0.020	5.33170	0.018
64	5.37012	5.35725	0.240	5.35743	0.237
65	5.40014	5.39589	0.079	5.39627	0.072
66	5.43224	5.43571	0.064	5.43599	0.069
67	5.45845	5.45699	0.027	5.45728	0.021
68	5.49232	5.49778	0.099	5.49816	0.106
69	5.54920	5.55358	0.079	5.55405	0.087
70	5.58061	5.58871	0.145	5.58914	0.153

TABLE VIII: Mn₃Ge sample A (regular shape)

Index	f_{exp} (MHz)	RPR		SMI		FEM	
		f_{calc} (MHz)	diff (%)	f_{calc} (MHz)	diff (%)	f_{calc} (MHz)	diff (%)
1	0.96469	0.95542	-	0.95544	-	0.95531	-
2	1.31011	1.31762	-	1.31764	-	1.31751	-
3	1.46748	1.46874	-	1.46876	-	1.46855	-
4	1.50955	1.50952	0.002	1.50951	0.002	1.50947	0.005
5	1.56402	1.56137	0.169	1.56136	0.170	1.56127	0.176
6	1.57830	1.57952	0.077	1.57951	0.077	1.57945	0.073
7	1.58425	1.60049	1.015	1.60051	1.016	1.60029	1.002
8	1.60141	1.61340	0.743	1.61340	0.743	1.61327	0.735
9	1.60582	1.61949	0.845	1.61951	0.846	1.61938	0.838
10	1.78631	1.80175	0.857	1.80177	0.858	1.80162	0.850
11	1.82036	1.81183	0.471	1.81182	0.471	1.81169	0.478
12	1.87303	1.87322	0.010	1.87322	0.010	1.87313	0.005
13	1.94132	1.93235	0.464	1.93233	0.465	1.93222	0.471
14	1.95112	1.95456	0.176	1.95455	0.175	1.95451	0.173
15	2.03329	2.02996	0.164	2.02997	0.164	2.02986	0.169
16	2.09609	2.08355	0.602	2.08353	0.603	2.08339	0.610
17	2.10555	2.10872	0.150	2.10867	0.148	2.10854	0.142
18	2.14587	2.12376	1.041	2.12373	1.043	2.12363	1.047
19	2.16239	2.17045	0.371	2.17041	0.369	2.17050	0.374
20	2.16541	2.17570	0.473	2.17572	0.474	2.17548	0.463
21	2.25310	2.26434	0.496	2.26437	0.497	2.26423	0.491
22	2.32002	2.30809	0.517	2.30807	0.518	2.30797	0.522
23	2.37049	2.35061	0.846	2.35060	0.846	2.35052	0.849
24	2.38275	2.38340	0.027	2.38330	0.023	2.38334	0.024
25	2.43586	2.41898	0.698	2.41896	0.699	2.41890	0.701
26	2.46256	2.47420	0.471	2.47422	0.471	2.47413	0.468
27	2.47301	2.47498	0.080	2.47498	0.080	2.47483	0.073
28	2.52384	2.55083	1.058	2.55069	1.053	2.55063	1.051
29	2.55464	2.57203	0.676	2.57205	0.677	2.57190	0.671
30	2.57758	2.59117	0.524	2.59118	0.525	2.59105	0.520
31	2.61331	2.62284	0.363	2.62282	0.363	2.62273	0.359
32	2.65457	2.64939	0.196	2.64940	0.195	2.64940	0.195
33	2.71919	2.72259	0.125	2.72258	0.124	2.72248	0.121
34	2.75160	2.74615	0.198	2.74616	0.198	2.74602	0.203
35	2.78098	2.77733	0.131	2.77734	0.131	2.77722	0.135
36	2.84224	2.83905	0.112	2.83904	0.113	2.83904	0.113
37	2.86041	2.86306	0.092	2.86298	0.090	2.86289	0.086
38	2.87166	2.86844	0.112	2.86847	0.111	2.86843	0.113
39	2.91103	2.92610	0.515	2.92611	0.516	2.92617	0.518
40	2.93140	2.92769	0.127	2.92770	0.126	2.92756	0.131
41	2.93455	2.93191	0.090	2.93190	0.090	2.93189	0.091
42	2.94156	2.94237	0.027	2.94237	0.028	2.94228	0.024
43	3.04438	3.05124	0.225	3.05123	0.224	3.05109	0.220
44	3.10644	3.09616	0.332	3.09616	0.332	3.09622	0.330
45	3.12912	3.13303	0.125	3.13303	0.125	3.13297	0.123
46	3.19343	3.17795	0.487	3.17796	0.487	3.17801	0.485
47	3.21141	3.21040	0.031	3.21041	0.031	3.21032	0.034
48	3.28658	3.28210	0.136	3.28212	0.136	3.28219	0.134
49	3.30955	3.29828	0.342	3.29828	0.342	3.29851	0.335
50	3.31565	3.32261	0.209	3.32261	0.209	3.32258	0.209
51	3.35754	3.37386	0.484	3.37387	0.484	3.37382	0.482
52	3.38287	3.37789	0.147	3.37786	0.148	3.37795	0.146
53	3.44121	3.45795	0.484	3.45795	0.484	3.45796	0.484
54	3.47190	3.46067	0.324	3.46069	0.324	3.46107	0.313
55	3.49421	3.48695	0.208	3.48694	0.208	3.48696	0.208
56	3.49812	3.50059	0.071	3.50057	0.070	3.50061	0.071
57	3.49964	3.51232	0.361	3.51236	0.362	3.51229	0.360
58	3.54746	3.53238	0.427	3.53237	0.427	3.53259	0.421
59	3.57278	3.56487	0.222	3.56488	0.222	3.56526	0.211
60	3.58496	3.57191	0.365	3.57191	0.365	3.57200	0.363
61	3.58767	3.59720	0.265	3.59714	0.263	3.59709	0.262

Table 8 continued on next page.

Table 8 continued.

Index	f_{exp} (MHz)	RPR		SMI		FEM	
		f_{calc} (MHz)	diff (%)	f_{calc} (MHz)	diff (%)	f_{calc} (MHz)	diff (%)
62	3.60231	3.60308	0.022	3.60311	0.022	3.60304	0.020
63	3.60760	3.60521	0.066	3.60521	0.066	3.60540	0.061
64	3.61308	3.60655	0.181	3.60655	0.181	3.60663	0.179
65	3.61436	3.61431	0.001	3.61432	0.001	3.61455	0.005
66	3.61865	3.62068	0.056	3.62069	0.057	3.62084	0.060
67	3.64765	3.64158	0.167	3.64152	0.168	3.64153	0.168
68	3.67018	3.64580	0.669	3.64580	0.669	3.64602	0.663
69	3.71718	3.70179	0.416	3.70179	0.416	3.70203	0.409
70	3.72327	3.72386	0.016	3.72386	0.016	3.72412	0.023
71	3.78761	3.79633	0.230	3.79635	0.230	3.79659	0.237
72	3.81140	3.80554	0.154	3.80556	0.153	3.80579	0.147
73	3.84430	3.82293	0.559	3.82295	0.559	3.82310	0.554
74	3.86988	3.84886	0.546	3.84885	0.546	3.84915	0.539
75	3.91723	3.91340	0.098	3.91339	0.098	3.91352	0.095
76	3.94563	3.92345	0.565	3.92345	0.565	3.92395	0.552
77	3.97908	3.97784	0.031	3.97787	0.030	3.97802	0.027
78	3.99942	3.99986	0.011	3.99985	0.011	4.00031	0.022
79	4.01915	4.00900	0.253	4.00903	0.252	4.00943	0.242
80	4.03495	4.02355	0.284	4.02355	0.283	4.02443	0.262
81	4.04595	4.06045	0.357	4.06046	0.357	4.06074	0.364
82	4.05758	4.06567	0.199	4.06558	0.197	4.06568	0.199
83	4.06491	4.08637	0.525	4.08631	0.524	4.08631	0.524
84	4.0780	4.09008	0.295	4.09004	0.294	4.09015	0.297

TABLE IX: Mn₃Ge sample B (irregular shape)

Index	f_{exp} (MHz)	SMI		FEM	
		f_{calc} (MHz)	diff (%)	f_{calc} (MHz)	diff (%)
1	0.77100	0.72927	-	0.72932	-
2	1.08478	1.06421	-	1.06356	-
3	1.22382	1.21029	-	1.21031	-
4	1.33437	1.32618	0.618	1.32623	0.614
5	1.44953	1.43028	1.346	1.43030	1.344
6	1.60718	1.59563	0.723	1.59565	0.722
7	1.86078	1.84572	0.816	1.84544	0.831
8	1.88524	1.88848	0.172	1.88804	0.148
9	2.02059	2.01970	0.044	2.01929	0.064
10	2.06617	2.03724	1.420	2.03660	1.452
11	2.12700	2.11597	0.521	2.11593	0.523
12	2.30712	2.29890	0.358	2.29885	0.360
13	2.33951	2.33223	0.312	2.33215	0.316
14	2.44134	2.43977	0.064	2.43948	0.076
15	2.48376	2.48460	0.034	2.48477	0.040
16	2.66501	2.66902	0.150	2.66862	0.135
17	2.75780	2.74510	0.463	2.74453	0.484
18	2.78254	2.78677	0.152	2.78699	0.160
19	2.83647	2.82217	0.507	2.82196	0.514
20	2.97943	2.99342	0.467	2.99356	0.472
21	3.01159	3.01770	0.203	3.01823	0.220
22	3.07402	3.09174	0.573	3.09132	0.560
23	3.13148	3.13824	0.215	3.13768	0.198
24	3.16311	3.17632	0.416	3.17606	0.408
25	3.24362	3.25436	0.330	3.25461	0.338
26	3.25447	3.27058	0.492	3.27034	0.485
27	3.30929	3.30305	0.189	3.30309	0.188
28	3.40908	3.42759	0.540	3.42754	0.539
29	3.46136	3.46796	0.190	3.46799	0.191
30	3.53828	3.52248	0.449	3.52213	0.459
31	3.58063	3.59778	0.477	3.59745	0.468
32	3.64885	3.64490	0.108	3.64495	0.107
33	3.70451	3.68606	0.500	3.68572	0.510

Table 9 continued on next page.

Table 9 continued.

Index	f_{exp} (MHz)	SMI		FEM	
		f_{calc} (MHz)	diff (%)	f_{calc} (MHz)	diff (%)
34	3.73124	3.74476	0.361	3.74458	0.356
35	3.77514	3.78817	0.344	3.78828	0.347
36	3.81664	3.81972	0.081	3.82010	0.091
37	3.84659	3.86236	0.408	3.86303	0.426
38	3.89301	3.90315	0.260	3.90408	0.283
39	3.92147	3.92013	0.034	3.92011	0.035
40	4.00155	4.01985	0.455	4.01957	0.448
41	4.05232	4.04810	0.104	4.04792	0.109
42	4.07279	4.07673	0.096	4.07692	0.101
43	4.11185	4.10555	0.154	4.10515	0.163
44	4.16568	4.12779	0.918	4.12750	0.925
45	4.17169	4.15185	0.478	4.15181	0.479
46	4.23171	4.23428	0.061	4.23422	0.059
47	4.25632	4.26175	0.127	4.26195	0.132
48	4.28696	4.29318	0.145	4.29333	0.148
49	4.33501	4.33233	0.062	4.33252	0.057
50	4.39232	4.39776	0.124	4.39806	0.131
51	4.44617	4.44492	0.028	4.44480	0.031
52	4.45932	4.45990	0.013	4.45953	0.005
53	4.47269	4.48323	0.235	4.48383	0.248
54	4.50973	4.51226	0.056	4.51274	0.067
55	4.54993	4.53911	0.239	4.53896	0.242
56	4.57564	4.59124	0.340	4.59160	0.348
57	4.61763	4.59924	0.400	4.59942	0.396
58	4.64177	4.63850	0.070	4.63892	0.061
59	4.67340	4.67170	0.036	4.67168	0.037
60	4.67725	4.71140	0.725	4.71268	0.752
61	4.74328	4.72813	0.320	4.72823	0.318
62	4.75405	4.76937	0.321	4.76985	0.331
63	4.78548	4.79885	0.279	4.79964	0.295
64	4.83816	4.84783	0.199	4.84855	0.214
65	4.87454	4.89056	0.328	4.89094	0.335
66	4.89770	4.89955	0.038	4.89976	0.042
67	4.91976	4.92224	0.050	4.92262	0.058
68	4.94198	4.93395	0.163	4.93404	0.161
69	4.97544	4.95930	0.326	4.95855	0.341
70	5.00234	4.98595	0.329	4.98635	0.321
71	5.05521	5.05121	0.079	5.05153	0.073
72	5.06222	5.07826	0.316	5.07871	0.325
73	5.10734	5.10605	0.025	5.10572	0.032
74	5.14001	5.15663	0.322	5.15649	0.320
75	5.17375	5.18850	0.284	5.18928	0.299
76	5.20031	5.19720	0.060	5.19750	0.054
77	5.22839	5.23149	0.059	5.23154	0.060
78	5.24876	5.27701	0.535	5.27763	0.547
79	5.31483	5.33671	0.410	5.33550	0.387
80	5.35238	5.35144	0.018	5.35154	0.016
81	5.36938	5.36972	0.006	5.36912	0.005
82	5.37790	5.40947	0.584	5.40967	0.587
83	5.41390	5.42943	0.286	5.42989	0.295
84	5.43467	5.44317	0.156	5.44304	0.154

TABLE X: UTe₂ sample A SMI fit results

Index	300 K			4 K		
	f_{exp} (MHz)	f_{calc} (MHz)	diff (%)	f_{exp} (MHz)	f_{calc} (MHz)	diff (%)
1	0.64645	0.64254	-	0.66344	0.65765	-
2	0.80333	0.80092	-	0.81724	0.81425	-
3	0.86443	0.85869	-	0.87702	0.87984	-
4	1.09564	1.09407	0.143	1.11952	1.12080	0.114
5	1.18679	1.18992	0.263	1.21970	1.21818	0.125

Table 10 continued on next page.

Table 10 continued.

Index	300 K			4 K		
	f_{exp} (MHz)	f_{calc} (MHz)	diff (%)	f_{exp} (MHz)	f_{calc} (MHz)	diff (%)
6	1.32441	1.32471	0.023	1.34208	1.34680	0.350
7	1.34023	1.33357	0.499	1.36327	1.35737	0.435
8	1.49544	1.49019	0.353	1.51789	1.51792	0.002
9	1.56441	1.57149	0.450	1.59618	1.60073	0.284
10	1.64031	1.64096	0.040	1.67269	1.67216	0.032
11	1.67848	1.67996	0.088	1.71445	1.71359	0.050
12	1.71675	1.71182	0.288	1.75060	1.74551	0.291
13	1.77448	1.77473	0.014	1.80806	1.80856	0.028
14	1.83771	1.83767	0.002	1.87151	1.87196	0.024
15	1.86861	1.86685	0.094	1.90573	1.90183	0.205
16	1.93964	1.93352	0.317	1.97323	1.97067	0.130
17	2.02902	2.02240	0.327	2.06927	2.06282	0.313
18	2.06086	2.06388	0.146	2.09666	2.10371	0.335
19	2.13401	2.13646	0.115	2.17374	2.17693	0.147
20	2.18310	2.17778	0.244	2.23096	2.22600	0.223
21	2.21720	2.21601	0.054	2.26583	2.25830	0.334
22	2.25887	2.25321	0.251	2.30249	2.29602	0.282
23	2.27636	2.28024	0.170	2.32310	2.32435	0.054
24	2.33423	2.33367	0.024	2.37609	2.37215	0.166
25	2.35896	2.35370	0.223	2.40235	2.40166	0.029
26	2.37195	2.37131	0.027	2.41002	2.41040	0.016
27	2.40361	2.39962	0.166	2.46079	2.45405	0.275
28	2.45741	2.45189	0.225	2.50592	2.50395	0.079
29	2.47653	2.47529	0.050	2.51386	2.52139	0.299
30	2.49726	2.49516	0.085	2.55527	2.55033	0.194
31	2.53119	2.53407	0.113	2.58793	2.58510	0.109
32	2.56841	2.57293	0.176	2.61987	2.62518	0.202
33	2.58945	2.58640	0.118	2.64506	2.64006	0.189
34	2.67652	2.67401	0.094	2.72662	2.72716	0.020
35	2.69934	2.70106	0.064	2.75414	2.75458	0.016
36	2.70867	2.71641	0.285	2.76160	2.76697	0.194
37	2.75772	2.76163	0.142	2.81381	2.81674	0.104
38	2.80315	2.80522	0.073	2.85929	2.86408	0.167
39	2.83790	2.83401	0.137	2.88995	2.88518	0.165
40	2.84413	2.84397	0.006	2.89806	2.89733	0.025
41	2.85740	2.85678	0.022	2.91031	2.91158	0.044
42	2.89809	2.90021	0.073	2.95404	2.95353	0.017
43	2.91204	2.90687	0.178	2.96297	2.95926	0.125
44	2.93294	2.93629	0.114	2.98892	2.98868	0.008
45	2.97064	2.96887	0.060	3.03454	3.03881	0.140
46	2.98750	2.98376	0.125	3.04986	3.04773	0.070
47	3.04099	3.04359	0.086	3.10384	3.10431	0.015
48	3.05451	3.05513	0.020	3.11878	3.11603	0.088
49	3.07129	3.06617	0.167	3.12869	3.12381	0.156
50	3.11543	3.11631	0.028	3.17516	3.18070	0.174
51	3.14348	3.14681	0.106	3.21205	3.20841	0.113
52	3.16609	3.16333	0.087	3.23373	3.23001	0.115
53	3.19312	3.19392	0.025	3.25821	3.25521	0.092
54	3.21950	3.22107	0.049	3.28885	3.29187	0.092
55	3.26064	3.26213	0.046	3.32549	3.32873	0.097
56	3.27367	3.27710	0.105	3.33381	3.33748	0.110
57	3.28431	3.28793	0.110	3.35277	3.35414	0.041
58	3.33902	3.33560	0.103	3.39969	3.39764	0.060
59	3.37665	3.38210	0.161	3.44137	3.44067	0.020
60	3.38263	3.38841	0.171	3.44466	3.45563	0.317
61	3.40724	3.40264	0.135	3.47399	3.46879	0.150
62	3.42588	3.41984	0.176	3.48688	3.48075	0.176
63	3.46878	3.46450	0.123	3.52655	3.52462	0.055
64	3.48772	3.48306	0.134	3.55491	3.55194	0.084
65	3.49884	3.50575	0.197	3.56459	3.57159	0.196
66	3.51096	3.51080	0.005	3.58054	3.57953	0.028

Table 10 continued on next page.

Table 10 continued.

Index	300 K			4 K		
	f_{exp} (MHz)	f_{calc} (MHz)	diff (%)	f_{exp} (MHz)	f_{calc} (MHz)	diff (%)
67	3.54860	3.55098	0.067	3.61868	3.62048	0.050
68	3.56768	3.57417	0.182	3.64321	3.64728	0.112
69	3.57963	3.58351	0.108	3.65177	3.65702	0.144
70	3.59151	3.59154	0.001	3.66315	3.66157	0.043
71	3.63037	3.63146	0.030	3.70535	3.70318	0.059
72	3.66135	3.66185	0.014	3.73498	3.73249	0.067
73	3.67686	3.67367	0.087	3.75129	3.74617	0.137
74	3.70093	3.69729	0.098	3.77215	3.77270	0.015
75	3.72551	3.71979	0.154	3.79478	3.78954	0.138
76	3.74072	3.74038	0.009	3.81853	3.81297	0.146
77	3.75135	3.75430	0.079	3.82596	3.82515	0.021
78	3.76556	3.76595	0.010	3.83940	3.83786	0.040
79	3.77374	3.77640	0.071	3.84028	3.84954	0.240
80	3.81529	3.81717	0.049	3.89424	3.89363	0.016
81	3.84139	3.83861	0.072	3.91424	3.91245	0.046
82	3.85843	3.85711	0.034	3.93674	3.93303	0.094
83	3.87490	3.88271	0.201	3.94923	3.95735	0.205
84	3.89786	3.89296	0.126	3.97082	3.96312	0.194
85	3.90314	3.90305	0.002	3.98043	3.98563	0.130
86	3.91220	3.92250	0.263	3.98665	3.99710	0.261
87	3.94153	3.93803	0.089	4.01442	4.01238	0.051
88	3.99297	3.98031	0.318	4.06185	4.05116	0.264
89	3.99436	3.99491	0.014	4.07113	4.06908	0.050
90	4.00126	4.01160	0.258	4.07942	4.08544	0.147
91	4.03760	4.03141	0.154	4.11408	4.10575	0.203
92	4.07137	4.07176	0.010	4.15105	4.14854	0.061
93	4.08673	4.08572	0.025	4.16596	4.16925	0.079
94	4.11792	4.11397	0.096	4.19784	4.19441	0.082
95	4.12896	4.13582	0.166	4.20427	4.21294	0.206
96	4.14529	4.15212	0.164	4.22149	4.22953	0.190
97	4.15242	4.15367	0.030	4.23333	4.23415	0.019
98	4.17297	4.17074	0.053	4.24888	4.24690	0.047
99	4.18994	4.18888	0.025	4.27899	4.27740	0.037
100	4.20373	4.21285	0.216	4.28904	4.29176	0.064
101	4.22958	4.23006	0.011	4.30977	4.31112	0.031
102	4.24199	4.24296	0.023	4.32438	4.32504	0.015
103	4.25360	4.25075	0.067	4.33687	4.33486	0.046
104	4.28642	4.28345	0.069	4.36950	4.36567	0.088
105	4.30657	4.30624	0.008	4.39228	4.39207	0.005
106	4.31547	4.31995	0.104	4.40638	4.40694	0.013
107	4.34118	4.34193	0.017	4.42091	4.42370	0.063
108	4.34935	4.35598	0.152	4.43621	4.44172	0.124
109	4.36295	4.36176	0.027	4.44922	4.44494	0.096
110	4.37974	4.37984	0.002	4.46691	4.46202	0.110
111	4.39652	4.38614	0.237	4.47881	4.46618	0.283
112	4.40482	4.41073	0.134	4.48982	4.49513	0.118
113	4.42003	4.41888	0.026	4.49809	4.50730	0.204
114	4.42672	4.42968	0.067	4.51862	4.51611	0.055
115	4.44940	4.46193	0.281	4.53519	4.54067	0.121
116	4.46937	4.47430	0.110	4.55608	4.55307	0.066
117	4.48235	4.48380	0.032	4.56374	4.56785	0.090
118	4.50482	4.50569	0.019	4.59148	4.59609	0.100
119	4.50733	4.51327	0.132	4.59729	4.60078	0.076
120	4.52413	4.52782	0.081	4.60960	4.61562	0.131
121	4.53911	4.54276	0.080	4.62762	4.63458	0.150
122	4.56333	4.56602	0.059	4.64820	4.65923	0.237
123	4.57367	4.57286	0.018	4.66121	4.66642	0.112
124	4.60540	4.60303	0.051	4.69278	4.69228	0.011
125	4.61532	4.62032	0.108	4.70740	4.71043	0.064
126	4.62818	4.62519	0.065	4.71517	4.71609	0.020
127	4.63514	4.63026	0.105	4.72725	4.71991	0.155

Table 10 continued on next page.

Table 10 continued.

Index	300 K			4 K		
	f_{exp} (MHz)	f_{calc} (MHz)	diff (%)	f_{exp} (MHz)	f_{calc} (MHz)	diff (%)
128	4.64194	4.64199	0.001	4.73331	4.73754	0.089
129	4.66690	4.66430	0.056	4.75924	4.75618	0.064
130	4.66790	4.66597	0.041	4.76674	4.75845	0.174
131	4.69246	4.68730	0.110	4.78743	4.78038	0.147
132	4.70527	4.71080	0.118	4.80128	4.80542	0.086
133	4.72046	4.73008	0.203	4.81305	4.82061	0.157
134	4.75051	4.75395	0.072	4.84664	4.84559	0.022
135	4.75900	4.76169	0.057	4.85021	4.85330	0.064
136	4.76976	4.77384	0.085	4.86402	4.86321	0.017
137	4.77918	4.77950	0.007	4.87531	4.87473	0.012
138	4.79086	4.79493	0.085	4.88149	4.88582	0.089
139	4.80450	4.80244	0.043	4.89785	4.89637	0.030
140	4.81875	4.81484	0.081	4.91309	4.90863	0.091
141				4.93822	4.94346	0.106
142				4.95627	4.95918	0.059
143				4.96168	4.96342	0.035
144				4.98300	4.98143	0.032
145				4.98846	4.99420	0.115
146				4.99438	5.00516	0.215
147				5.01215	5.01596	0.076
148				5.02882	5.03051	0.034
149				5.04591	5.05275	0.135
150				5.06142	5.06270	0.025

TABLE XI: UTe₂ sample B SMI fit results

Index	300 K			4 K		
	f_{exp} (MHz)	f_{calc} (MHz)	diff (%)	f_{exp} (MHz)	f_{calc} (MHz)	diff (%)
1	0.84871	0.84530	-	-	0.86336	-
2	0.85476	0.85964	-	0.87178	0.87760	-
3	0.95597	0.95934	-	0.97940	0.97664	-
4	1.06829	1.07054	0.211	1.09070	1.09144	0.068
5	1.11300	1.11809	0.455	1.14186	1.14466	0.245
6	1.20905	1.20671	0.194	1.23137	1.23157	0.017
7	1.27627	1.27098	0.417	1.29907	1.29403	0.389
8	1.30668	1.30995	0.249	1.33148	1.33537	0.291
9	1.33404	1.33004	0.301	1.36093	1.35854	0.176
10	1.42356	1.41859	0.350	1.45056	1.44869	0.129
11	1.46580	1.46271	0.211	1.49748	1.49177	0.383
12	1.50799	1.51040	0.160	1.54068	1.53982	0.055
13	1.56016	1.56319	0.194	1.60017	1.59666	0.219
14	1.60842	1.60909	0.042	1.64060	1.64240	0.110
15	1.74339	1.74654	0.180	1.77974	1.78031	0.032
16	1.78190	1.79245	0.589	1.81928	1.82974	0.572
17	1.80619	1.80062	0.309	1.85079	1.84454	0.338
18	1.87349	1.87715	0.195	1.90804	1.91116	0.163
19	1.90921	1.90783	0.072	1.94151	1.94324	0.089
20	1.94674	1.94192	0.249	1.98817	1.98452	0.184
21	2.00583	2.00390	0.096	2.04584	2.04287	0.145
22	2.03086	2.02432	0.323	2.08163	2.06424	0.843
23	2.07441	2.07694	0.122	2.11713	2.11986	0.129
24	2.11673	2.11636	0.018	2.15876	2.15825	0.023
25	2.16436	2.16975	0.248	2.20781	2.21144	0.164
26	2.18929	2.19732	0.366	2.23165	2.23803	0.285
27	2.22146	2.23034	0.398	2.26420	2.27408	0.434
28	2.24902	2.25516	0.272	2.29215	2.30158	0.409
29	2.30961	2.31141	0.078	2.35312	2.36037	0.307
30	2.32704	2.33105	0.172	2.37484	2.38182	0.293
31	2.35294	2.34928	0.156	2.40488	2.39906	0.243
32	2.39058	2.38243	0.342	2.43754	2.43052	0.289
33	2.45167	2.45230	0.026	2.50518	2.50352	0.066

Table 11 continued on next page.

Table 11 continued.

Index	300 K			4 K		
	f_{exp} (MHz)	f_{calc} (MHz)	diff (%)	f_{exp} (MHz)	f_{calc} (MHz)	diff (%)
34	2.48080	2.48028	0.021	2.53395	2.53062	0.132
35	2.50531	2.51258	0.289	2.56447	2.56033	0.162
36	2.53711	2.53137	0.227	2.58939	2.58027	0.353
37	2.55822	2.55799	0.009	2.61119	2.61444	0.124
38	2.57543	2.57151	0.153	2.62709	2.61993	0.273
39	2.62322	2.61786	0.205	2.67498	2.67047	0.169
40	2.63654	2.63938	0.107	2.69240	2.69640	0.148
41	2.70147	2.70243	0.036	2.75821	2.75649	0.062
42	2.75069	2.74791	0.101	2.80820	2.80488	0.119
43	2.77773	2.77670	0.037	2.83486	2.83282	0.072
44	2.80230	2.80822	0.211	2.85674	2.86124	0.157
45	2.81487	2.81788	0.107	2.87440	2.87460	0.007
46	2.83215	2.82934	0.099	2.88578	2.88481	0.034
47	2.84899	2.84838	0.021	2.90458	2.90969	0.176
48	2.88217	2.89120	0.312	2.94201	2.95391	0.403
49	2.90566	2.89877	0.238	2.96333	2.95683	0.220
50	2.91847	2.91501	0.119	2.98089	2.97713	0.126
51	2.92686	2.92827	0.048	2.98623	2.98834	0.071
52	2.95275	2.95268	0.002	3.01343	3.01194	0.049
53	3.00092	2.99982	0.037	3.06884	3.06684	0.065
54	3.02153	3.02916	0.252	3.08283	3.08955	0.217
55	3.05196	3.04553	0.211	3.11517	3.10990	0.170
56	3.08793	3.08125	0.217	3.14866	3.14128	0.235
57	3.11778	3.11646	0.042	3.17516	3.17388	0.040
58	3.14639	3.14909	0.085	3.20090	3.21009	0.286
59	3.16393	3.16218	0.055	3.22399	3.22528	0.040
60	3.19065	3.18964	0.032	3.25573	3.25409	0.050
61	3.19738	3.20093	0.111	3.25919	3.26248	0.101
62	3.20855	3.20654	0.063	3.26893	3.27039	0.045
63	3.23995	3.24651	0.202	3.30460	3.31243	0.236
64	3.27675	3.28070	0.120	3.34246	3.34638	0.117
65	3.29429	3.29614	0.056	3.35998	3.36766	0.228
66	3.30627	3.30639	0.004	3.37335	3.37228	0.032
67	3.31057	3.31439	0.115	3.37764	3.38353	0.174
68	3.36154	3.35425	0.217	3.42970	3.42873	0.028
69	3.38338	3.38541	0.060	3.45002	3.45428	0.123
70	3.39821	3.39330	0.145	3.47019	3.46476	0.157
71	3.41174	3.41505	0.097	3.48083	3.48357	0.079
72	3.45929	3.45902	0.008	3.52382	3.53192	0.229
73	3.47176	3.46545	0.182	3.54420	3.53371	0.297
74	3.48530	3.48412	0.034	3.54503	3.55265	0.215
75	3.49764	3.50499	0.210	3.56748	3.57564	0.228
76	3.53011	3.52311	0.199	3.60152	3.59743	0.114
77	3.54142	3.54333	0.054	3.60770	3.61281	0.141
78	3.57423	3.56654	0.216	3.64468	3.63636	0.229
79	3.59789	3.59154	0.177	3.67123	3.66223	0.246
80	3.61091	3.60483	0.169	3.68580	3.68020	0.152
81	3.61554	3.61654	0.028	3.69086	3.68809	0.075
82	3.64128	3.64220	0.025	3.71976	3.71920	0.015
83	3.65329	3.65013	0.087	3.72490	3.72397	0.025
84	3.67338	3.67530	0.052	3.74859	3.75135	0.074
85	3.68955	3.68592	0.099	3.76758	3.75922	0.222
86	3.70091	3.69442	0.176	3.77312	3.76937	0.099
87	3.70751	3.70096	0.177	3.78014	3.77801	0.056
88	3.72219	3.72029	0.051	3.80089	3.80091	0.001
89	3.74091	3.74401	0.083	3.81654	3.81771	0.030
90	3.78334	3.78100	0.062	3.85825	3.85286	0.140
91	3.79235	3.79414	0.047	3.86975	3.87632	0.169
92	3.82170	3.81175	0.261	3.89582	3.88778	0.207
93	3.83868	3.83761	0.028	3.91696	3.91147	0.140
94	3.84736	3.85549	0.211	3.92636	3.93085	0.114

Table 11 continued on next page.

Table 11 continued.

Index	300 K			4 K		
	f_{exp} (MHz)	f_{calc} (MHz)	diff (%)	f_{exp} (MHz)	f_{calc} (MHz)	diff (%)
95	3.86778	3.85859	0.238	3.94426	3.93995	0.109
96	3.87212	3.87332	0.031	3.94801	3.95067	0.067
97	3.87768	3.88691	0.237	3.95793	3.96709	0.231
98	3.91034	3.91012	0.006	3.99414	3.98805	0.153
99	3.94800	3.93730	0.272	4.02057	4.01300	0.189
100	3.96335	3.96620	0.072	4.04528	4.04773	0.060
101	3.96897	3.97227	0.083	4.05160	4.05507	0.086
102	3.98406	3.98991	0.147	4.06035	4.06586	0.135
103	4.00409	4.00748	0.085	4.08358	4.08793	0.106
104	4.02581	4.02391	0.047	4.10434	4.10784	0.085
105	4.02903	4.03805	0.223	4.10898	4.11773	0.213
106	4.06773	4.06629	0.035	4.14695	4.14959	0.063
107	4.08881	4.08893	0.003	4.17275	4.17261	0.003
108	4.09297	4.09859	0.137	4.17465	4.18384	0.220
109	4.10732	4.10027	0.172	4.19085	4.18721	0.087
110	4.11337	4.11117	0.053	4.19902	4.19819	0.020
111	4.12319	4.12322	0.001	4.20850	4.20670	0.043
112	4.13332	4.14047	0.173	4.21682	4.22095	0.098
113	4.14011	4.14630	0.149	4.22597	4.23065	0.111
114	4.17361	4.16635	0.174	4.25691	4.24756	0.220
115				4.28207	4.28041	0.039
116				4.29878	4.29524	0.082
117				4.31342	4.31466	0.029
118				4.32482	4.32771	0.067

-
- [1] C. Girod, C. R. Stevens, A. Huxley, E. D. Bauer, F. B. Santos, J. D. Thompson, R. M. Fernandes, J.-X. Zhu, F. Ronning, P. F. S. Rosa, and S. M. Thomas, Thermodynamic and electrical transport properties of UTe₂ under uniaxial stress, *Physical Review B* **106**, L121101 (2022).
- [2] A. Shragai, F. Theuss, G. Grissonnanche, and B. J. Ramshaw, Rapid method for computing the mechanical resonances of irregular objects, *The Journal of the Acoustical Society of America* **153**, 119 (2023).
- [3] R. Storn and K. Price, Differential Evolution – A Simple and Efficient Heuristic for global Optimization over Continuous Spaces, *Journal of Global Optimization* **11**, 341 (1997).
- [4] P. Virtanen, R. Gommers, T. E. Oliphant, M. Haberland, T. Reddy, D. Cournapeau, E. Burovski, P. Peterson, W. Weckesser, J. Bright, S. J. van der Walt, M. Brett, J. Wilson, K. J. Millman, N. Mayorov, A. R. J. Nelson, E. Jones, R. Kern, E. Larson, C. J. Carey, I. Polat, Y. Feng, E. W. Moore, J. VanderPlas, D. Laxalde, J. Perktold, R. Cimrman, I. Henriksen, E. A. Quintero, C. R. Harris, A. M. Archibald, A. H. Ribeiro, F. Pedregosa, P. van Mulbregt, and SciPy 1.0 Contributors, SciPy 1.0: Fundamental Algorithms for Scientific Computing in Python, *Nature Methods* **17**, 261 (2020).
- [5] B. J. Ramshaw, A. Shekhter, R. D. McDonald, J. B. Betts, J. N. Mitchell, P. H. Tobash, C. H. Mielke, E. D. Bauer, and A. Migliori, Avoided valence transition in a plutonium superconductor, *Proceedings of the National Academy of Sciences of the United States of America* **112**, 3285 (2015).
- [6] A. Migliori, J. L. Sarrao, W. M. Visscher, T. M. Bell, M. Lei, Z. Fisk, and R. G. Leisure, Resonant ultrasound spectroscopic techniques for measurement of the elastic moduli of solids, *Physica B: Condensed Matter* **183**, 1 (1993).
- [7] F. F. Balakirev, S. M. Ennaceur, R. J. Migliori, B. Maiorov, and A. Migliori, Resonant ultrasound spectroscopy: The essential toolbox, *Review of Scientific Instruments* **90**, 121401 (2019).
- [8] W. M. Visscher, A. Migliori, T. M. Bell, and R. A. Reinert, On the normal modes of free vibration of inhomogeneous and anisotropic elastic objects, *The Journal of the Acoustical Society of America* **90**, 2154 (1991).